JCB Journal of Cell Biology

ARTICLE

Ca^{2+}-induced release of IQSEC2/BRAG1 autoinhibition under physiological and pathological conditions

Guanhua Bai[1,2*], Hao Li[3,4*], Pengwei Qin[3,4], Yiqing Guo[3,4], Wanfa Yang[2], Yinmiao Lian[3,4], Fei Ye[2], Jianxin Chen[5,6], Meiling Wu[1], Ruifeng Huang[1], Jinsong Li[5,6], Youming Lu[3,4], and Mingjie Zhang[1,2,7]

IQSEC2 (aka BRAG1) is a guanine nucleotide exchange factor (GEF) highly enriched in synapses. As a top neurodevelopmental disorder risk gene, numerous mutations are identified in *Iqsec2* in patients with intellectual disabilities accompanied by other developmental, neurological, and psychiatric symptoms, though with poorly understood underlying molecular mechanisms. The atomic structures of IQSECs, together with biochemical analysis, presented in this study reveal an autoinhibition and Ca^{2+}-dependent allosteric activation mechanism for all IQSECs and rationalize how each identified *Iqsec2* mutation can alter the structure and function of the enzyme. Transgenic mice modeling two pathogenic variants of *Iqsec2* (R359C and Q801P), with one activating and the other inhibiting the GEF activity of the enzyme, recapitulate distinct clinical phenotypes in patients. Our study demonstrates that different mutations on one gene such as *Iqsec2* can have distinct neurological phenotypes and accordingly will require different therapeutic strategies.

Introduction

Iqsec2 is located at chromosome Xp11.22 and is a member of a family of three genes (*Iqsec1-3*). It was initially proposed as a candidate X-linked intellectual disability (XLID) gene in a study of a patient with a de novo chromosomal translocation (Morleo et al., 2008). Since then, >100 pathogenic variants of *Iqsec2* have been reported, leading to both syndromic (e.g., seizures, speech deficits, autistic or other psychiatric behaviors, etc.) and non-syndromic forms of intellectual disability (ID; Accogli et al., 2020; Barrie et al., 2020; Levy et al., 2023; Lopergolo et al., 2021; Mignot et al., 2019; Radley et al., 2019; Shoubridge et al., 2019, 2022; Wayhelova et al., 2020). These mutations are spread throughout the protein-coding sequence of the gene. As *Iqsec2* is an X-linked gene, hemizygous males are more affected by mutations than heterozygous females. However, there is an increasing number of cases where heterozygous female patients suffer from severe ID and/or seizures similar to male patients carrying the same *Iqsec2* mutations (Mignot et al., 2019; Shoubridge et al., 2019). Mutations in *Iqsec1* and *Iqsec3* have also been recently identified in families with autosomal-recessive IDs in consanguineous populations (Ansar et al., 2019; Monies et al., 2019), highlighting the critical role of *Iqsecs* in proper brain development and function in humans.

Although an increasing number of ID patients bearing mutations in *Iqsecs* (particularly *Iqsec2*) have been identified, there is still a lack of knowledge regarding the genotype–phenotype relationship in *Iqsec* variants. *Iqsec1-3* encodes guanine nucleotide exchange factors (GEFs), IQSEC1-3, also known as BRAG1-3, for the ARF family of small GTP-binding proteins. Each gene has multiple splice variants that are generally expressed in a tissue-specific manner. Among the three family members, IQSEC1 is ubiquitously expressed in different tissues, including the brain (Someya et al., 2001). IQSEC2 and IQSEC3 are highly enriched in the nervous system. In the brain, IQSEC1 and IQSEC2 are enriched in the postsynaptic densities of excitatory synapses, and IQSEC3 is specifically expressed in inhibitory synapses (Lowenthal et al., 2015; Murphy et al., 2006; Uezu et al., 2016; Um et al., 2016). In neurons, the IQSEC1/2 proteins are known to be involved in the activity-dependent removal of α-amino-3-

[1]School of Life Sciences, Southern University of Science and Technology, Shenzhen, China; [2]Division of Life Science, State Key Laboratory of Molecular Neuroscience, Hong Kong University of Science and Technology, Kowloon, China; [3]Department of Pathophysiology, School of Basic Medicine and Tongji Medical College, Huazhong University of Science and Technology, Wuhan, China; [4]The Institute for Brain Research, Collaborative Innovation Center for Brain Science, Huazhong University of Science and Technology, Wuhan, China; [5]State Key Laboratory of Cell Biology, Shanghai Key Laboratory of Molecular Andrology, CAS Center for Excellence in Molecular Cell Science, Shanghai Institute of Biochemistry and Cell Biology, Chinese Academy of Sciences, University of Chinese Academy of Sciences, Shanghai, China; [6]School of Life Science and Technology, Shanghai Tech University, Shanghai, China; [7]Greater Bay Biomedical Innocenter, Shenzhen Bay Laboratory, Shenzhen, China.

*G. Bai and H. Li contributed equally to this paper. Correspondence to Youming Lu: lym@hust.edu.cn; Mingjie Zhang: zhangmj@sustech.edu.cn.

hydroxy-5-methyl-4-isoxazole-propionic acid receptors (AMPARs) from synapses, thereby modulating synaptic activities (Brown et al., 2016; Myers et al., 2012; Scholz et al., 2010). The structures of the Sec7-PH tandem of IQSEC1 have been solved, providing valuable insights for interpreting IQSEC mutations occurring in the catalytic domain of the enzyme (Aizel et al., 2013). However, how the enzymatic activities of IQSECs are regulated remains unclear. Patients with different mutations present a broad spectrum of clinical phenotypes (Barrie et al., 2020; Levy et al., 2019; Mignot et al., 2019; Shoubridge et al., 2019, 2022), emphasizing the need to understand the impact of variant mutations on the functions of IQSECs to fully comprehend disease etiology caused by *Iqsec* mutations and to develop potential therapeutic methods for brain disorders with greater precision.

In this study, we determined the structures of apo-calmodulin (CaM)-bound forms of IQSEC1 and IQSEC2 and conducted an extensive biochemical and functional analysis of IQSEC2 and its variants. Our research revealed that IQSECs adopt an autoinhibited conformation that can be released upon elevation of Ca^{2+} concentration. Furthermore, our study revealed that missense mutations in different domains, R359C in the IQ-motif and Q801P in the Sec7 domain of IQSEC2, had opposite impacts on the GEF activity of the enzyme, a finding that can rationalize distinct phenotypic and synaptic alterations observed in mice carrying the two mutants. Remarkably, the crystal structures of the enzymes solved in this work can interpret almost all *Iqsec2* missense mutations identified in ID patients.

Results

The IQ-motif/apo-CaM complex is coupled with the catalytic Sec7-PH tandem in IQSECs

The IQSECs are characterized by the presence of an IQ-like motif in addition to the catalytic Sec7-PH tandem (Murphy et al., 2006; Sakagami et al., 2008). Both regions are highly conserved among the three isoforms and throughout evolution (Fig. 1 A). Notably, the IQ-like motif contains ∼60 residues (Fig. 1 A), which is much longer than ∼20 residues for a canonical CaM-binding IQ-motif (Bähler and Rhoads, 2002). Previous reports have pointed out an ambiguous relationship between the CaM interaction and calcium-dependent activation of IQSECs (Myers et al., 2012; Rogers et al., 2019). Moreover, patients with missense mutations in the IQ-motif have been found to exhibit overlapping but distinct phenotypes compared to those with variants in the Sec7 domain. Thus, to understand the role of the IQ-motif in regulating IQSECs' GEF activity and its action mechanism, we started our investigation by directly measuring the interactions between IQ-motif/CaM complexes and the Sec7-PH tandem.

However, the isolated IQ-motifs of all three IQSECs have extremely low solubility, which makes them unsuitable for biochemical studies. To address this, we coexpressed each IQ-motif with CaM, which allowed for the purification of homogeneous IQ/CaM complexes under both Ca^{2+}-free and Ca^{2+}-bound conditions. Analytical gel filtration chromatographic analysis showed that the IQ-motifs of all three IQSECs could bind to Ca^{2+}-free and Ca^{2+}-saturated CaM, forming stable complexes (Fig. 1 B; and Fig. S1, A and B). Furthermore, gel-filtration analysis showed that the IQ/apo-CaM complex of each IQSEC can bind to their respective Sec7-PH tandem (Fig. 1 C; and Fig. S1, A and B). The isothermal titration calorimetry (ITC)-based assay revealed that the IQ/apo-CaM complex of IQSEC2/3 binds to the Sec7-PH tandem of the enzymes with K_D of ∼2.0–3.6 μM (Fig. 1 D and Fig. S1 C). It is important to note that the intramolecular interaction between IQ/apo-CaM and Sec7-PH in each IQSEC should be much stronger than the intermolecular bindings measured by ITC. Thus, it can be inferred that in the absence of Ca^{2+}, the IQ-motif of IQSECs binds to apo-CaM and folds together with the Sec7-PH tandem, leading IQSECs to adopt a closed conformation.

Ca^{2+} binding to CaM allosterically releases the closed conformation of IQSECs

Interestingly, the IQ/Ca^{2+}-CaM complex showed no detectable binding to the Sec7-PH tandem in all IQSECs (Fig. 1, C and D; and Fig. S1, A–C). This finding suggests that the elevation of Ca^{2+} concentration causes the IQ/CaM complex to dissociate from the catalytic Sec7-PH tandem, leading to the release of the closed conformation of IQSECs.

To investigate the Ca^{2+}-induced allosteric opening of IQSECs, we used NMR spectroscopy with IQSEC3 as the model due to its favorable sample behavior. Although full-length IQSECs could not be purified, we successfully purified an IQSEC3 fusion protein by linking the IQ-motif and the Sec7-PH tandem with a 12-residue flexible linker (four repeats of "GGS," referred to as IQ∼Sec7PH; Fig. S1 D). On the gel filtration column, the IQ∼Sec7PH/apo-CaM complex eluted at a similar volume to the IQ/apo-CaM complex bound to the Sec7-PH tandem (Fig. S1 D), indicating that the IQ-motif, together with apo-CaM, interacted with the Sec7-PH tandem intramolecularly forming a monomeric complex.

To simplify NMR spectra, we selectively ^{15}N-labeled CaM in the IQ∼Sec7PH/CaM complex by replacing the unlabeled CaM using ion-exchange chromatography. The ^{1}H-^{15}N heteronuclear single quantum coherence (HSQC) spectrum of the ^{14}N_IQ∼Sec7PH/^{15}N_apo-CaM complex showed very low signals (Fig. S1 E, orange). This observation is consistent with the tight coupling of IQ/apo-CaM with the Sec7-PH tandem such that the peaks from CaM became very broad due to forming a large molecular weight complex. Upon the addition of Ca^{2+}, the peaks of CaM in the complex become dramatically sharper (Fig. S1 E, blue), indicating the release of Ca^{2+}-CaM from coupling to the Sec7-PH tandem. Importantly, the peaks of Ca^{2+}-CaM in the IQ∼Sec7PH/CaM complex nicely overlapped with the peaks of Ca^{2+}-CaM in the complex with the IQ-motif only (Fig. 1 E and Fig. S1 F), directly revealing that, in the presence of Ca^{2+}, CaM still binds to the IQ-motif, but the IQ/CaM complex is fully released from the catalytic Sec7-PH tandem.

Using purified IQ∼Sec7PH of IQSEC3, we measured its binding affinities to apo- and Ca^{2+}-CaM. Apo-CaM binds to IQ∼Sec7PH with an extremely strong affinity (K_D ∼1 nM; Fig. 1 F), indicating that apo-CaM, the IQ-motif, and Sec7-PH are

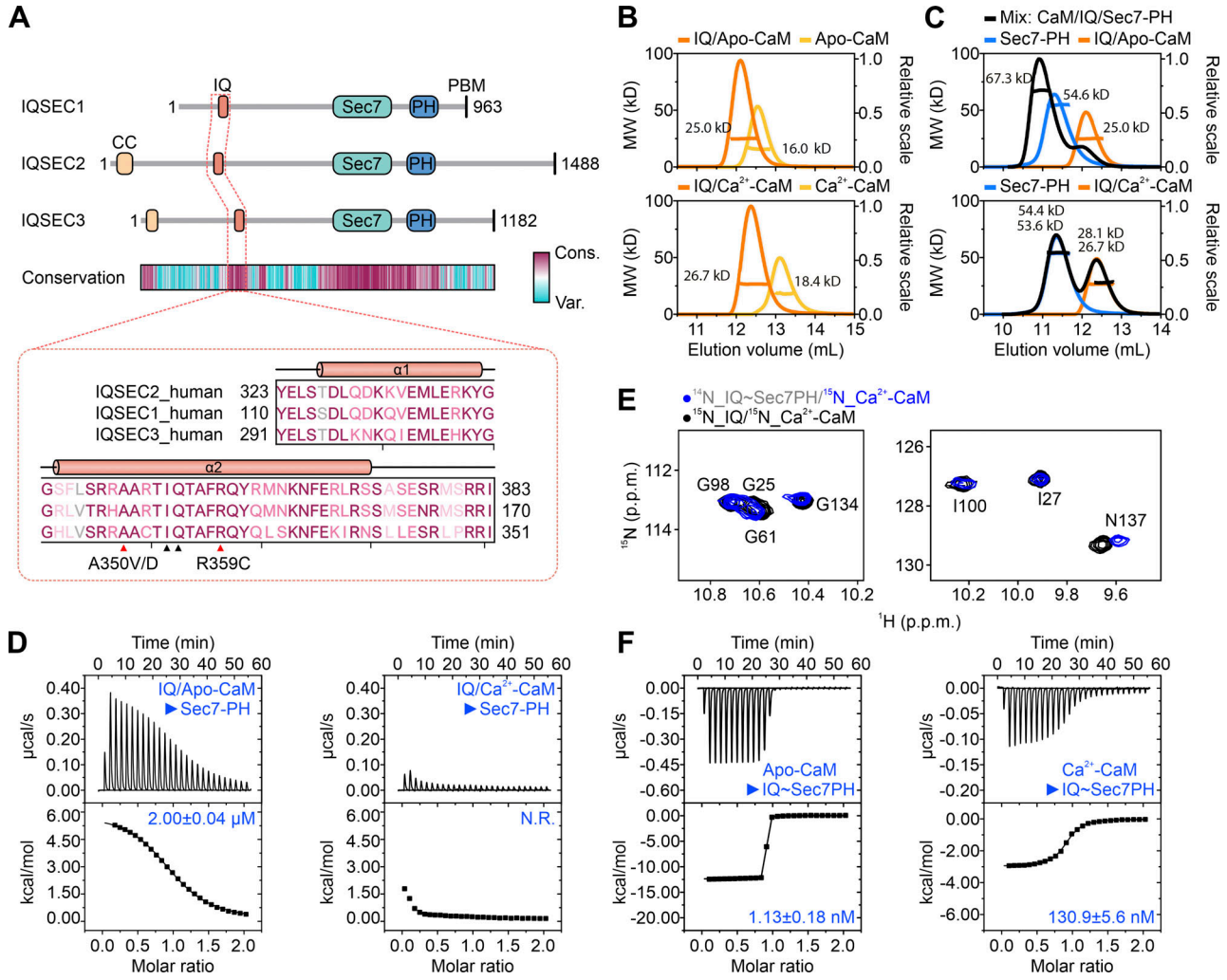

Figure 1. **The IQ-motif/CaM complex is coupled with the Sec7-PH tandem in IQSECs and dissociated by Ca^{2+}. (A)** Schematic diagrams showing the domain organization and amino acid sequence conservation of IQSECs from different species. Amino acid sequences of the region encompassing the extended IQ-motif of IQSECs are aligned. The predicted α-helices in the extended IQ-motif are labeled. Residues in the IQ-motif of IQSEC2 found to be mutated in ID patients are indicated. Cons., conserved; Var., variable. **(B)** The size-exclusion chromatography coupled with multiangle light scattering (SEC-MALS) analysis shows that the IQ-motif and CaM formed homogenous stabled complexes both in the absence and presence of Ca^{2+}. **(C)** The SEC-MALS analysis shows that the IQ-motif/CaM complex and the Sec7-PH tandem of IQSEC3 formed stable complexes in the absence of Ca^{2+} and dissociated in the presence of Ca^{2+}. **(D)** The ITC curve of 200 μM IQ-motif/CaM complex titrating into 20 μM Sec7-PH protein of IQSEC3 in the absence and presence of Ca^{2+}. N.R., fitting is not reliable due to very weak binding. **(E)** Superposition plot of a small region of the ^{1}H, ^{15}N HSQC spectra of the $^{14}N\_IQ\sim Sec7PH/^{15}N\_Ca^{2+}$-CaM complexes (blue) and $^{15}N\_IQ/^{15}N\_Ca^{2+}$-CaM complexes (black). The full ^{1}H, ^{15}N HSQC spectra are shown in Fig. S1 F. The assignments of the peaks corresponding to the $^{15}N\_Ca^{2+}$-CaM are labeled. **(F)** The ITC curve of 100 μM CaM titrating into 10 μM IQ~Sec7PH protein of IQSEC3 in the absence and presence of Ca^{2+}.

coupled together very tightly. The measured K_D presumably represents the combined bindings of apo-CaM to the IQ-motif and of the resulting complex binding to the Sec7-PH tandem. In contrast, Ca^{2+}-CaM binds to IQ~Sec7PH with an affinity of ~100-fold lower than apo-CaM does (Fig. 1 F). Since the IQ/Ca^{2+}-CaM complex is completely uncoupled from Sec7-PH, the K_D value of Ca^{2+}-CaM binding to IQ~Sec7PH likely represents the K_D of the IQ/Ca^{2+}-CaM complex.

Crystal structure of the apo-CaM/IQ/Sec7-PH ternary complex

To understand the molecular basis governing the Ca^{2+}-regulated allosteric transition of IQSECs, we tried to determine the crystal structure of the apo-CaM/IQ/Sec7-PH complex. Among all the trials, the ternary complex of IQSEC1 yielded well-diffracted (to 2.00-Å resolution) crystals. Crystals of the corresponding IQSEC2 complex diffracted to 3.48 Å and the IQSEC3 complex diffracted even more poorly and thus was not further analyzed (Table 1 and Fig. 2). The overall apo-CaM/IQ/Sec7-PH complex structures of IQSEC1 and IQSEC2 are essentially identical (Fig. S2, A and B), so we use the high-resolution IQSEC1 structure for the following detailed analysis.

The overall structure of the apo-CaM/IQ/Sec7-PH complex is highly compact and with three layers: the bottom Sec7-PH layer, the middle IQ-motif layer, and the top apo-CaM layer (Fig. 2, A–C). The extended IQ-motif, spanning 60 residues, adopts an "L-shaped" structure comprising two α-helices (termed as pre-IQ helix and IQ-helix corresponding to α1 and α2 in Fig. 1 A, respectively) connected with a sharp turn formed by two

Table 1. **Statistics of crystallographic data collection and refinement**

Data collection	**IQSEC1_Apo-CaM/IQ/Sec7-PH**	**IQSEC2_Apo-CaM/IQ/Sec7-PH**
Space group	P 21 21 21	P 1 21 1
Wavelength (Å)	0.97891	1.099
Unit cell parameters		
a, b, c (Å)	67.010, 81.436, 124.762	61.132, 76.274, 68.502
α, β, γ (°)	90.000, 90.000, 90.000	90.000, 101.04, 90.000
Resolution range (Å)	50.00–2.00 (2.03–2.00)	56.08–3.48 (3.53–3.48)
No. of unique reflections	46,959 (2,345)	7,998 (389)
Redundancy	10.1 (10.3)	3.4 (3.5)
I/σ	27.26 (3.38)	13.74 (2.66)
Completeness (%)	99.8 (100.0)	99.1 (99.5)
R_{merge}[a] (%)	6.8 (48.4)	9.1 (37.5)
$CC_{1/2}$[b]	0.988 (0.940)	0.992 (0.857)
Structure refinement		
Resolution (Å)	2.00	3.48
R_{work}[c] (%)	19.78	26.06
R_{free}[d] (%)	25.23	35.14
Root-mean-square deviation		
Bonds (Å)	0.0072	0.0096
Angles (°)	0.78	1.6008
Average B factor (Å^2)	38.4	85.7
No. of atoms		
Protein	4,162	3,632
Ligand/ion	18	0
Water	268	3
B Factors (Å^2)		
Proteins	38.4	85.8
Ligand/ion	48.8	0
Water	36.9	37.8
Ramachandran plot (%)		
Preferred	96.89	98.6
Allowed	3.11	1.4
Outliers	0	0

Numbers in parentheses represent the values for the highest-resolution shell.
[a]$R_{merge} = \sum|I_i - \langle I\rangle|/\sum I_i$, where I_i is the intensity of the measured reflection and $\langle I\rangle$ is the mean intensity of all symmetry-related reflections.
[b]$CC_{1/2}$ was defined in Karplus and Diederichs (2012).
[c]$R_{work} = \sum w||F_{calc}| - |F_{obs}||/\sum|F_{obs}|$, where F_{obs} and F_{calc} are observed and calculated structure factors. W is a working dataset of about 95% of the total unique reflections randomly chosen and used for refinement.
[d]$R_{free} = \sum_T||F_{calc}| - |F_{obs}||/\sum|F_{obs}|$, where T is a test dataset of about 5% of the total unique reflections randomly chosen and set aside prior to refinement.

conserved Gly residues and an unstructured loop C-terminal to the IQ-helix. In addition to binding to apo-CaM, the extended IQ-motif interacts with the Sec7 and PH domains, burying a total of 1,572.6 Å^2 surface area. The residues from Sec7-PH responsible for binding to the IQ-motif and apo-CaM are highly conserved in all IQSEC family members and throughout the evolution (Fig. 2 B).

The complex structure provides an explanation for why the IQ-motifs in IQSECs are much longer than the canonical IQ-motifs. Biochemical validation experiments showed that removing either the pre-IQ helix (aa 113–131; human IQSEC1 numbering as in Fig. 1 A) or the post-IQ loop (aa 167–178) eliminated the binding between IQ/apo-CaM and the Sec7-PH tandem (Fig. 2 I). In the ternary complex, the conformation of the Sec7-PH tandem is essentially identical to that in the previously reported ARF1-bound IQSEC1 complex (PDB code: 4C0A; Aizel et al., 2013) with an r.m.s. deviation of 0.474 Å (Fig. S2 C). Surprisingly, only the C-lobe of apo-CaM binds to the elongated IQ-motif and the N-lobe of CaM projects away from the complex, and only three helices could be traced, presumably due to their conformational flexibility.

The interaction interface of the apo-CaM/IQ/Sec7-PH complex can be divided into five parts (Fig. 2, C–H): the interface between IQ and CaM (Site 1), between CaM and Sec7 domain (Site 2), between the pre-IQ helix and the Sec7-PH tandem (Site 3), between the IQ-helix and Sec7 (Site 4), and between the C-terminal loop of the IQ-motif and Sec7 (Site 5).

In Site 1 (Fig. 2 D), the CaM C-lobe adopts a semi-open conformation and binds to the hydrophobic residues from the IQ-helix as observed in other canonical IQ/apo-CaM interactions (Fig. S2 D). Two residues in the pre-IQ helix (K127 and Y128) also participate in binding to CaM. In contrast to the consensus IQ-motif sequence ("IQxxxRGxxxR"), the conserved Gly in the IQSEC1 IQ-motif is a Gln (Q147; Fig. S2 E), which sterically hinders the CaM N-lobe from binding to the IQ-helix. Additionally, the Arg at the end of the canonical IQ-motif is replaced by a Gln or Ser in the IQ-motif of IQSECs, which also disfavors the CaM N-lobe from binding (Fig. S2 E). Therefore, the N-lobe of apo-CaM floats outside of the ternary complex.

In addition to binding to the IQ-motif, CaM directly contacts several residues from the Sec7 domain of IQSEC1 (Site 2; Fig. 2 E). In Site 3, several residues form the pre-IQ helix and form hydrogen bonds with residues from the PH domain and the linker helix connecting the PH and Sec7 domains (Fig. 2 F). The IQ-helix extensively interacts with the Sec7 domain via hydrogen-bonding/charge and hydrophobic interactions (Fig. 2 G). Finally, residues from the post-IQ loop form several pairs of salt bridges with residues from the Sec7 domain (Site 5; Fig. 2 H).

To validate the role of the interactions shown in Fig. 2, D–H, we performed an extensive list of mutations for residues from both the IQ-motif and the Sec7-PH tandem. Substituting individual residue in each interaction site with a residue of a very different side chain property either weakened or even completely abolished the interaction between IQ/apo-CaM and the Sec7-PH tandem of IQSECs (Fig. 2 I).

Unfortunately, we were unable to obtain the crystal structure of Ca^{2+}-CaM in complex with the extended IQ-motif of IQSECs.

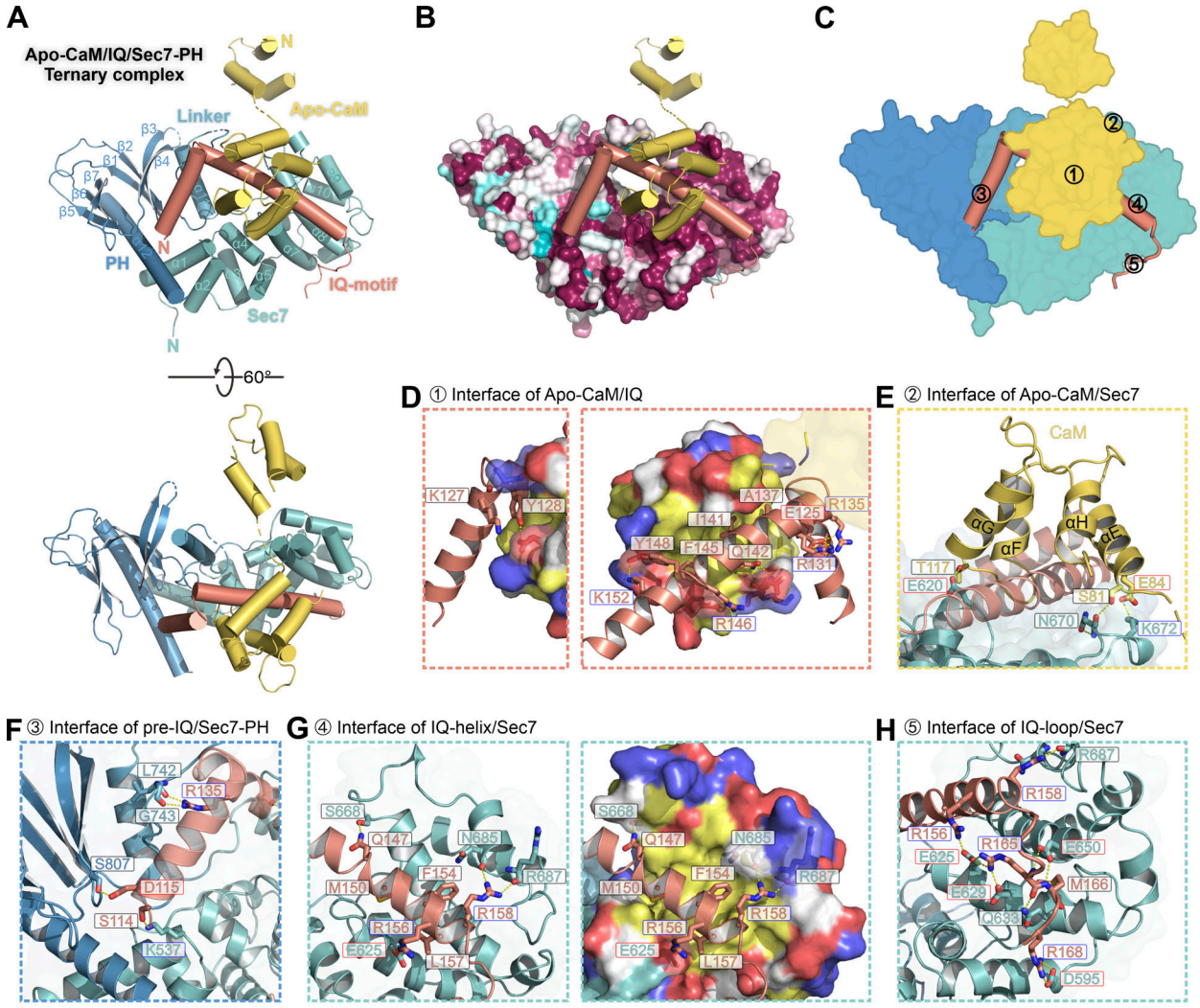

I

Structure validation summary

IQ/Apo-CaM	Sec7-PH K_D (μM)
WT	2.00±0.04

IQ/Apo-CaM_Mut	Sec7-PH K_D (μM)
Apo-CaM only	N.R.
IQ/Apo-CaM-C	10.06±0.18

IQ_helix/Apo-CaM	Sec7-PH K_D (μM)
α1: 86-130 (300-343)	N.D.
α2: 131-178 (344-391)	N.R.

IQ_Mut/Apo-CaM	Sec7-PH K_D (μM)
Y128A (341)	N.R.
R135A (348)	11.07±0.78
Q147A (360)	9.52±0.52
F154A (367)	N.R.
R156E (369)	12.72±0.83
R158A (371)	N.R.
R165E (378)	16.98±0.88
R168A (381)	6.37±0.41

Sec7-PH_Mut	IQ/Apo-CaM K_D (μM)
D595R (824)	12.27±0.65
E625R (854)	N.R.
E629R (858)	N.R.
Q633A (862)	8.40±0.22
D650A (879)	N.R.
F657A (886)	N.R.
L661A (890)	N.R.
K672E (901)	N.R.

The dissociation constant (K_D) is derived from ITC titration.
Number (in parentheses) indicating the amino acid position in hIQSEC1 (hIQSEC2).
N.R.: Very weak binding, fitting is not reliable.
N.D.: Not detectable.

Figure 2. **Structure of the apo-CaM/IQ/Sec7-PH ternary complex. (A)** Cartoon representation of the apo-CaM/IQ/Sec7-PH ternary complex structure of IQSEC1. **(B)** The amino acid conservation of IQSECs mapped to the surface of the Sec7-PH tandem structure. **(C)** Schematic diagram of the IQSEC1 apo-CaM/IQ/Sec7-PH complex showing five characteristic interfaces between apo-CaM/IQ and Sec7-PH as detailed in D–H. **(D)** The detailed interaction interface between the C-lobe of apo-CaM and the IQ-motif. Residues from the IQ-motif mediating critical interactions with CaM are drawn with the stick model. The surface of CaM is colored as follows: yellow, hydrophobic residues; blue, positively charged residues; red, negatively charged residues. **(E)** The interaction interface between the C-lobe of apo-CaM and the Sec7 domain. **(F)** The interaction interface between the pre-IQ helix and the Sec7-PH tandem. **(G)** The interaction interface between the IQ-helix and the Sec7 domain. The surface of the Sec7-PH tandem is colored with the same scheme as in D. **(H)** The interaction interface between the C-terminal loop of the IQ-motif and the Sec7 domain. **(I)** Summary of ITC-derived binding affinities between various IQ-motif proteins with different mutant forms of the Sec7-PH tandem for structural validation of the apo-CaM/IQ/Sec7-PH ternary complex. Each mutant protein was purified using the same method for the corresponding WT protein.

However, through NMR spectroscopy, we confirmed that both lobes of Ca^{2+}-CaM are involved in binding to the IQ-motif of IQSECs (Fig. S2, F and G). It is well known that CaM undergoes a significant conformational change upon Ca^{2+} binding (Zhang et al., 1995). Furthermore, for IQ-motifs that are known to bind to both apo- and Ca^{2+}-CaM, each lobe would engage the IQ-motif with a different orientation and position (relative to the IQ-helix) under Ca^{2+}-free and Ca^{2+}-saturated conditions (see Li et al. [2017] and refs therein). Given the extremely tight packing of the IQ-motif with both apo-CaM and the Sec7-PH tandem in the closed conformation of IQSECs (Fig. 2), Ca^{2+} binding to CaM would make IQ/Ca^{2+}-CaM complex incompatible with binding to Sec7-PH, thereby triggering the conformational opening of the enzyme.

Ca^{2+} relieves autoinhibition of IQSEC to stimulate its GEF activity

Comparison of the crystal structure of the apo-CaM/IQ/Sec7-PH complex determined here with that of the Sec7-PH tandem in complex with ARF1-GDP (PDB code: 4C0A [Aizel et al., 2013]) revealed that the ARF binding site on the Sec7 domain is entirely occluded by the IQ/apo-CaM complex (Fig. 3 A). Since the IQ/apo-CaM complex is tightly coupled to the Sec7-PH tandem, it can be inferred that in the absence of Ca^{2+}, the GEF activity of IQSECs is autoinhibited. Ca^{2+} binding to CaM triggers the dissociation of the IQ/CaM complex from the Sec7-PH tandem, thereby releasing the autoinhibited conformation of the enzyme. Therefore, a Ca^{2+}-induced (or synaptic activity-induced) IQSEC enzymatic activity regulation mechanism readily emerges. It is plausible that, while still attached to the IQ-motif under the Ca^{2+}-bound state, the IQSEC-bound CaM can rapidly respond to a decrease in Ca^{2+} concentration and revert the enzyme to its inactive state.

To investigate the regulation of IQSEC2 GEF activity by Ca^{2+}, we measured the enzymatic parameters of purified enzymes using a fluorescent-based assay (Fig. 3, B–D). Our results revealed that the ARF-GEF activity of the IQ~Sec7PH/apo-CaM complex was significantly suppressed compared with that of the Sec7-PH tandem (as measured by both k_{cat} and k_{cat}/K_M of each reaction). Upon the addition of Ca^{2+} to IQ~Sec7PH/CaM of IQSEC2, there was a significant increase in its GEF activity (Fig. 3, C and D), directly connecting with the Ca^{2+}-induced allosteric opening of the enzyme. We noted that in the presence of saturated Ca^{2+}, the GEF activity of IQSEC2 was about half of that of the Sec7-PH tandem, possibly indicating the existence of some transient intramolecular binding between IQ/Ca^{2+}-CaM complex with the catalytic Sec7-PH tandem.

Q801P mutation in the Sec7 domain abolished the intrinsic GEF activity of IQSEC2

To date, hundreds of different IQSEC2 pathogenic structural or intragenic coding variants have been reported (Accogli et al., 2020; Barrie et al., 2020; Lopergolo et al., 2021; Mignot et al., 2019; Radley et al., 2019; Shoubridge et al., 2019, 2022; Wayhelova et al., 2020; Fig. 3, E and F; and Fig. 4, A and B). The mutation sites are distributed throughout the entire IQSEC2. The majority of these mutations cause truncation of IQSEC2 either due to the introduction of stop codon directly or by indel mutation-induced frameshifts. Except for truncations leading to the removal of the C-terminal PBM of the enzyme, most of such mutations display severe clinical phenotypes likely due to mutation-induced loss of the mutant allele of the enzyme, which is due to non-functional truncated proteins or nonsense-mediated mRNA decays.

Interestingly, most pathogenic missense mutations are concentrated in the IQ-motif and the Sec7-PH tandem of IQSEC2. The structure of the CaM/IQ/Sec7-PH complex, together with the Ca^{2+}-dependent allosteric activation mechanism revealed in this study, allows us to systematically interpret the molecular basis underlying most of these identified mutations (Fig. 3, E and F; and Fig. 4, A–C). The majority of mutations found in the Sec7-PH tandem are located away from the IQ/Sec7-PH interface and can disrupt either the folding of Sec7-PH or its binding to the membrane (Fig. 3 F). Here, we take Q801P as an example. Q801 is located at the beginning of the α4 helix of the Sec7 domain, which is critical for stabilizing the active site conformation, including the catalytic Glu (E849) in the α6-α7 loop of the protein (Fig. 4 D). Replacing Q801 with Pro is expected to destabilize the α4 helix conformation and thus alter the active site conformation and impair the intrinsic catalytic activity of the enzyme. The Sec7-PH_Q801P tandem was shown to have the same binding property to both IQ/apo-CaM and IQ/Ca^{2+}-CaM as the wild-type (WT) Sec7-PH does (Fig. 4 C), suggesting the Ca^{2+}-regulated allosteric transition of the mutant protein remains intact. Precisely as predicted, the Q801P mutation resulted in a significantly decreased activity of the catalytic Sec7-PH tandem (Fig. 4 D), while the Q801P mutant of IQ~Sec7PH remained autoinhibited in the absence of Ca^{2+} and could be activated by increased Ca^{2+} concentration, even though the overall enzyme activity was significantly reduced (Fig. 4 D).

R359C and A350V/D in the IQ-motif impair Ca^{2+}-dependent allosteric regulation of IQSEC2

Several mutations in the IQSEC2 IQ-motif (e.g., A350V/D and R359C) have been identified in patients with broad disease phenotypes (Shoubridge et al., 2019). R359 ("A_{350}xxxIQxxxR_{359}QxxxxK") is at the position that is extremely conserved in all apo-CaM binding IQ-motifs (Fig. 1 A). R359 forms a pair of salt-bridge with E121 and a hydrogen bond with the backbone of K115 from CaM (Fig. 4 E). Replacing R359 with Cys dramatically weakened the interaction between IQSEC2 IQ-motif and apo-CaM but had less impact on Ca^{2+}-CaM binding (Fig. 4, C and F). Thus, the R359C mutation is predicted to have higher basal activity in the absence of Ca^{2+} due to the mutation-induced weakening of autoinhibition (Fig. 4, C and E). The rise of Ca^{2+} concentration would still activate the mutant enzyme. Consistent with the above structural analysis and biochemical binding data, the R359C mutant of IQ-Sec7PH in the presence of apo-CaM showed a higher GEF activity than the WT enzyme. The addition of Ca^{2+} further elevated the activity of the mutant enzyme, although there was only less than onefold activation instead of approximately fivefold activation for the WT enzyme (Fig. 4 E). Therefore, the R359C mutation of IQSEC2 leads to a "leaky" enzyme with higher basal activity, and the Ca^{2+}-regulated dynamic range of the GEF activity change is also reduced.

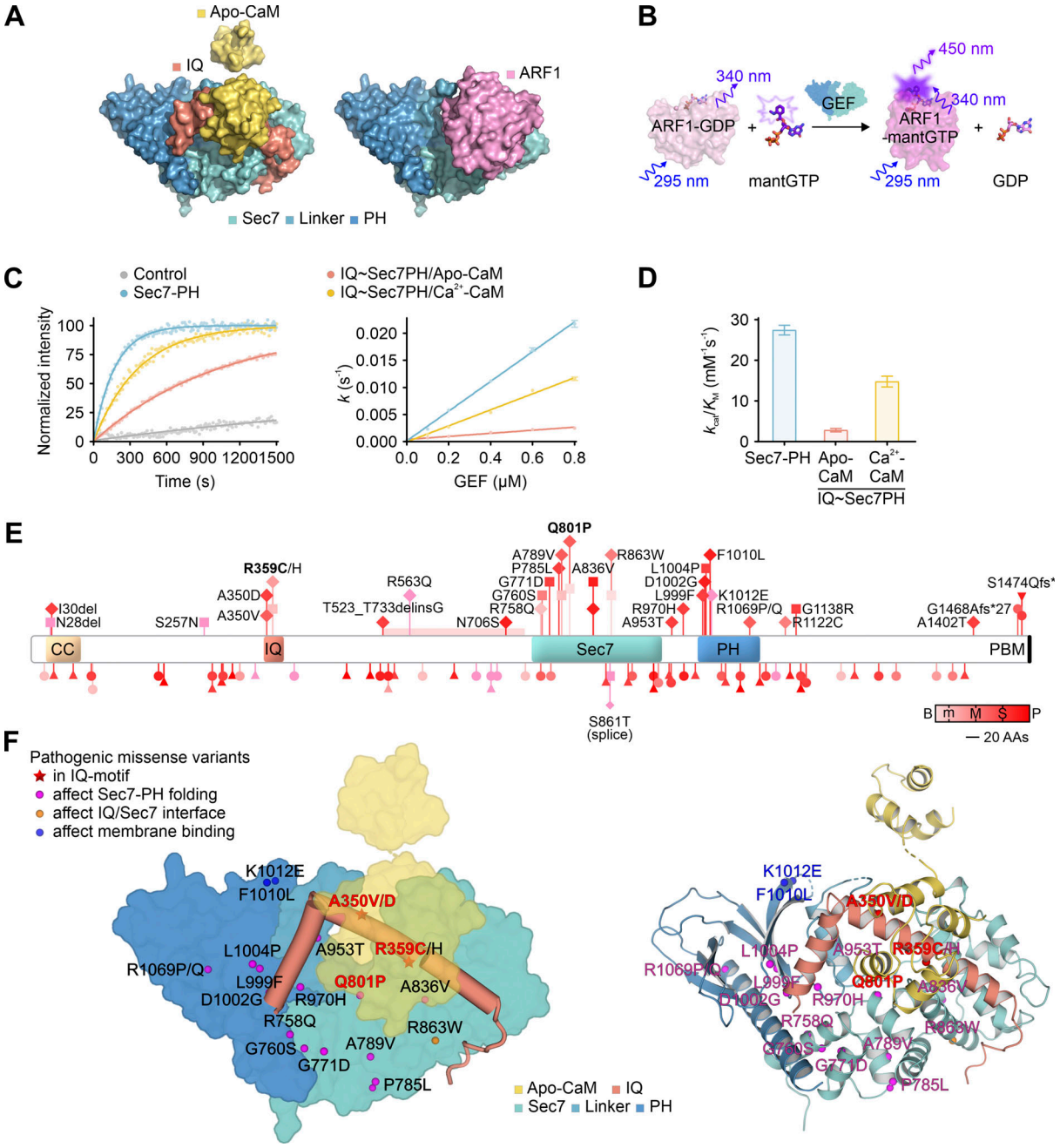

Figure 3. **Autoinhibition and Ca^{2+}-induced activation of IQSEC2. (A)** Comparison of the apo-CaM/IQ/Sec7-PH ternary complex structure with that of the ARF1/Sec7-PH complex (PDB accession no. 4C0A). **(B)** Schematic illustration of the fluorescent-based guanine nucleotide exchange assay used in this study. **(C)** Representative fluorescence kinetic curves for determining k_{obs} and plots of k_{obs} against GEF protein concentrations used to calculate k_{cat}/K_M. The kinetic traces were fitted with the one-phase exponential association model. Data are presented as mean ± SD from four repeated measurements. **(D)** The GEF activity (k_{cat}/K_M fit values) of IQSEC2 proteins in the absence and presence of Ca^{2+}. Bar graphs represent the mean ± SD of slopes obtained from linear regression analysis of data in C (right) at different conditions. **(E)** Summary of *Iqsec2* pathogenic missense variants and loss-of-function variants mapped to the schematic diagram of the longest isoform of the protein (GenBank ID NP_001104595.1). Predicted domain organization is drawn to scale: N-terminal coiled-coil (CC) domain, the IQ-motif (IQ), the Sec7 and Pleckstrin homology (PH) domains, and the C-terminal PDZ-binding motif (PBM). Diamond: missense variants present in affected males; square: missense variants present in affected females; triangle: loss-of-function variants present in affected males; dot: loss-of-function variants present in affected females. Variants are ranked by a red-colored scale against the severity of ID or developmental delay (DD): B, borderline; m, mild; M, moderate; S, severe; P, profound; pink: unknown. The p.R359C and p.Q801P variants in this study are labeled in bold. **(F)** Schematic diagram showing the distributions of pathogenic missense variants of IQSEC2 mapped to its structure using the surface (left) and ribbon diagram (right) models. The predicted (or experimentally demonstrated in the current study) impact of each mutation based on the structures of the IQSEC1 and IQSEC2 determined in this work are indicated with different colors and described in the figure.

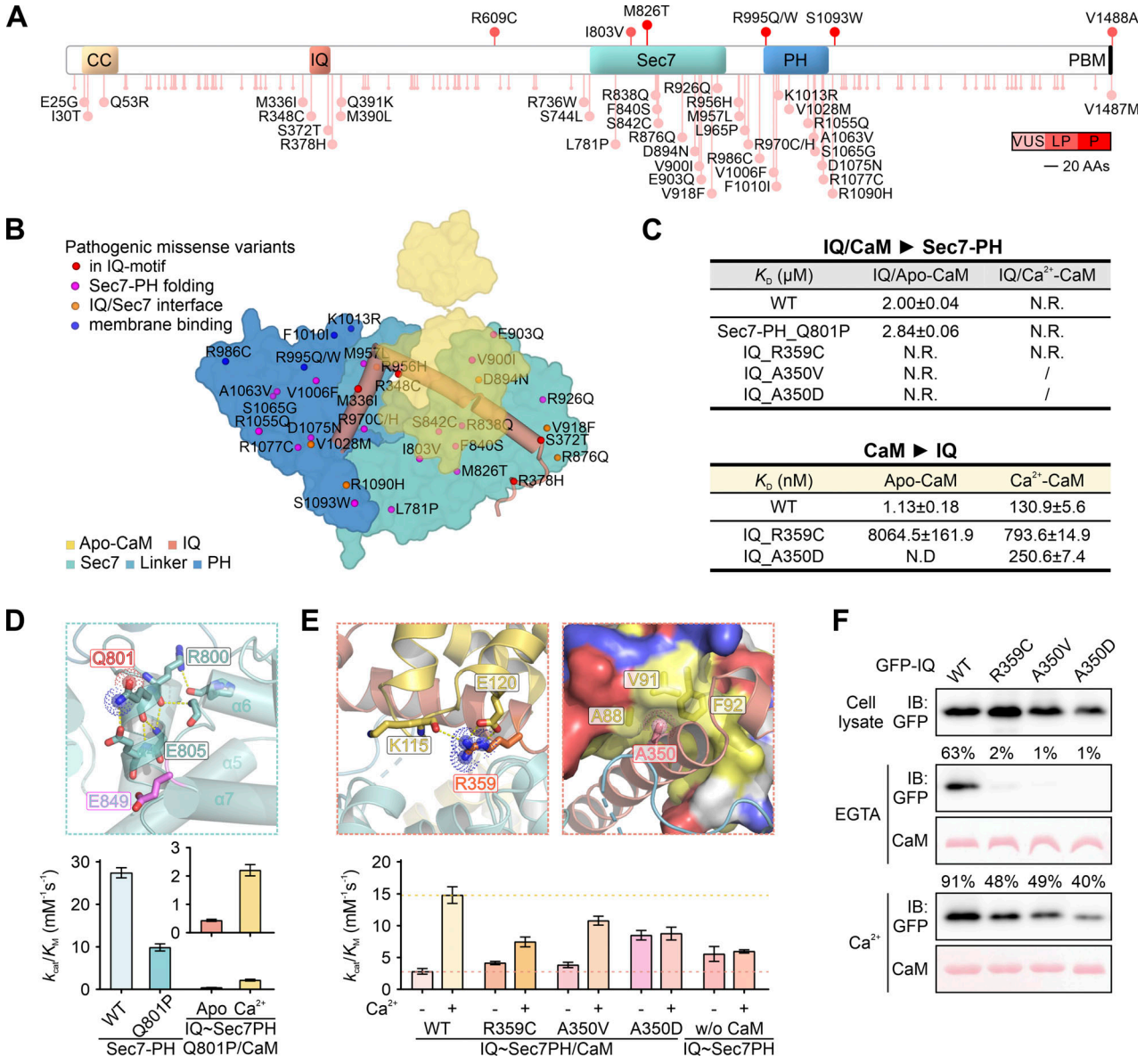

Figure 4. **Structural and biochemical analysis of missense mutations in IQSEC2. (A)** Summary of currently documented *Iqsec2* missense variants to the schematic diagram of the longest isoform (GenBank ID NP_001104595.1). Variants are ranked by red scale against the clinical significance: VUS, variants of unclear significance; LP, likely pathogenic; P, pathogenic. **(B)** Schematic diagram showing the distributions of all currently documented missense variants of IQSEC2 mapped to the structure of the protein. **(C)** Summary of how missense mutations affect the binding affinities between IQ-motif proteins with the Sec7-PH tandem or CaM in the absence and presence of Ca^{2+}. **(D and E)** The detailed interactions surrounding Q801, R359, and A350 of IQSEC2 as illustrated by the structure of the apo-CaM/IQ/Sec7-PH ternary complex. Bar graphs showing the GEF activity (k_{cat}/K_M values) of WT and the mutants of IQSEC2 in the absence and presence of Ca^{2+}. Data are presented as mean ± SD from four repeated measurements. **(F)** Representative pull-down assay showing weakened interactions between the mutant IQ-motif proteins of IQSEC2 and CaM both in the absence and presence of Ca^{2+}. The amount of protein eluted from the resin (relative to each input) is indicated above each lane. Source data are available for this figure: SourceData F4.

A350 is located at the beginning of the IQSEC2 IQ motif (Fig. 1 A) and is also highly conserved in apo-CaM binding IQ-motifs. A350 snuggly fits into the center of the hydrophobic surface of the CaM C-lobe (Fig. 4 E), explaining that either increasing the size of the sidechain (e.g., the A350V mutation) or changing the charge property of the residue (e.g., the A350D mutation) would impair the binding between the IQ-motif and apo-CaM (Fig. 4, C and F). Similar to the R359C mutation, A350V/D in the IQ-motif also weakens or abolishes its intramolecular coupling with the Sec7-PH tandem (Fig. 4 C), resulting in the A350V mutant of IQSEC2 displaying slightly elevated basal activity and the enzyme being less activated by Ca^{2+}. Also the A350D mutant of IQSEC2 displayed a much higher basal activity, which could no longer be further activated by the addition of Ca^{2+}, at an intermedial level approximate to the WT IQ~Sec7PH protein without CaM (Fig. 4 E). Notably, in agreement with the different Ca^{2+}-regulated dynamic ranges of the GEF activity, patients with the A350D mutation are known to have more severe disease phenotypes than patients with the A350V mutation (Shoubridge et al., 2019).

In a short summary, the above detailed structural and biochemical analysis revealed that different missense mutations in IQSEC2 can have distinct activity as well as Ca^{2+}-dependent allosteric regulation of the enzyme. Specifically, the Q801P mutation results in reduced intrinsic enzyme activity in both the basal and activated states and the mutation can be regarded as a loss of GEF activity of IQSEC2. However, the enzyme is still fully capable of responding to Ca^{2+}, and thus the mutant enzyme may still be able to function as an effective scaffold protein as the WT enzyme does. In contrast, the R359C and the A350V/D mutations are GEF activity gain-of-function mutations at the basal state. However, these mutant enzymes have much narrower Ca^{2+}-triggered GEF activation dynamic ranges.

Generation of IQSEC2 R359C and Q801P mice

The distinctly different biochemical impacts of various mutations within the same *Iqsec2* gene are likely responsible, at least in part, for the very different disease phenotypes observed in patients. Recently, *Iqsec2* knock-out mouse models were reported to produce some aspects of the human phenotypes (Mehta et al., 2021; Sah et al., 2020), but the molecular mechanism underlying the pathogenic phenotypes caused by different missense mutations cannot be explained by the total removal of *Iqsec2*. To further study the genotype–phenotype relationships of *Iqsec2* variants, we generated two knock-in mouse lines carrying the pathogenic missense mutations R359C or Q801P (Fig. S3 A), which were extensively characterized above.

IQSEC2 R359C and Q801P mutant mice were fertile and displayed no differences in body weight as compared with their respective WT control littermates (Fig. S3 B). The gross appearance, including the cellular structures in the cortex and the hippocampus from R359C and Q801P mutant mice, were also normal (Fig. S3, C–E), showing that R359C and Q801P mutations did not affect the brain structures and development.

Distinct synaptic phenotypes of the IQSEC2 R359C and Q801P mice

Endogenous IQSEC2 exhibited a widespread distribution in adult mouse brains, as shown by genetically tagging its N-terminal end with mScarlet (Fig. S3 F). Consistent with mRNA in situ hybridization and immunohistochemical analysis described previously (Sah et al., 2020; Sakagami et al., 2008), IQSEC2 is highly enriched throughout the forebrain, including the cerebral cortex and hippocampus. In the hippocampus, IQSEC2 is preferentially localized in both the CA1 and the molecular layer of the dentate gyrus (DG; Fig. S3 F).

To investigate the synaptic mechanisms underlying the R359C and the Q801P mutations, we assessed the synaptic transmissions of CA1 pyramidal neurons elicited by Schaffer-collateral stimulations in acute hippocampal slices. Whole-cell patch clamp recording of evoked excitatory postsynaptic currents (EPSCs) in response to elevated stimulus intensities revealed decreased synaptic responses in the Q801P neurons (Fig. 5, A and B). Consistently, the mean amplitude, but not the frequency of the spontaneous and miniature EPSCs in the Q801P neurons, was also significantly decreased (Fig. 5, C and D). In contrast, the basal synaptic strength of the R359C neurons was not altered (Fig. 5, A–D), which corroborates our structural findings suggesting that this mutation impairs Ca^{2+} sensitivity without affecting the basal synaptic transmission. No changes were observed in the spontaneous and miniature inhibitory postsynaptic currents (IPSCs) for both the R359C and the Q801P mice (Fig. S3, G and H). These results indicated that the Q801P, but not the R359C mutation, reduces the strength of the basal excitatory synaptic transmission.

Next, we set out to determine whether R359C and Q801P mutations impair activity-dependent synaptic plasticity, which has been widely considered as a cellular substrate of learning and memory. We measured evoked excitatory postsynaptic potentials (EPSPs) by delivering three consecutive episodes of brief high-frequency stimulation (HFS) after the baseline recording. We used this paradigm to examine the possible ceiling effects of the R359C and Q801P mutations on the induction and the expression of long-term potentiation (LTP). In control littermates and the Q801P mice (whose Ca^{2+}-dependent allosteric activation of IQSEC2 was preserved), there was an incremental trend in the slope of evoked EPSPs over the three successive HFS epochs, with each enhancement being less pronounced than its predecessor (Fig. 5, E and F). In contrast, the R359C mice, while showing a typical response to the inaugural HFS, displayed a stark deficit in generating further LTP following the second HFS (Fig. 5 E), alluding to a restricted modulation bandwidth and swift saturation of the synaptic response to Ca^{2+}. To further understand the synaptic implications of R359C and Q801P mutations, we evaluated the long-term depression (LTD) induced by applying low-frequency stimulation (LFS), a process demanding activity-dependent endocytosis of AMPARs. Interestingly, both the R359C (insensitive to the Ca^{2+} signal) and the Q801P (lacking Arf-GEF activity) mice showed impaired LTD (Fig. 5 G). These distinct synaptic phenotypes observed in IQSEC2 R359C and Q801P mutant mice, along with our prior structural–functional studies, paint a coherent picture of the specific biochemical and structural impacts these mutations have on synaptic transmission. With these insights, we are now primed to explore how these synaptic alterations may translate into broader impacts on animal behavior, which is a critical next step to gaining a more comprehensive understanding of the role of these IQSEC2 mutations in pathogenesis.

Distinct behavioral phenotypes of the IQSEC2 R359C and Q801P mice

The p.R359C and p.Q801P variants (human and mouse IQSEC2 are the same in their amino acid sequence lengths) are inherited and found in both male and female patients (Shoubridge et al., 2010). In addition to the different levels of ID in affected individuals, seizures and autistic traits are noted as well. Here, we recorded the spontaneous behaviors of the mice over 48 h in their home cage to screen natural behavioral patterns and to analyze locomotor activities as well as physical and mental conditions (Fig. S4 A). Compared with the WT littermates, the IQSEC2 R359C mutant mice exhibited overgrooming, which is often considered an autistic repetitive behavior, and the Q801P mutant mice spent less time sniffing, indicating that this mutation may alter the exploratory activity of the mice (Fig. S4 B).

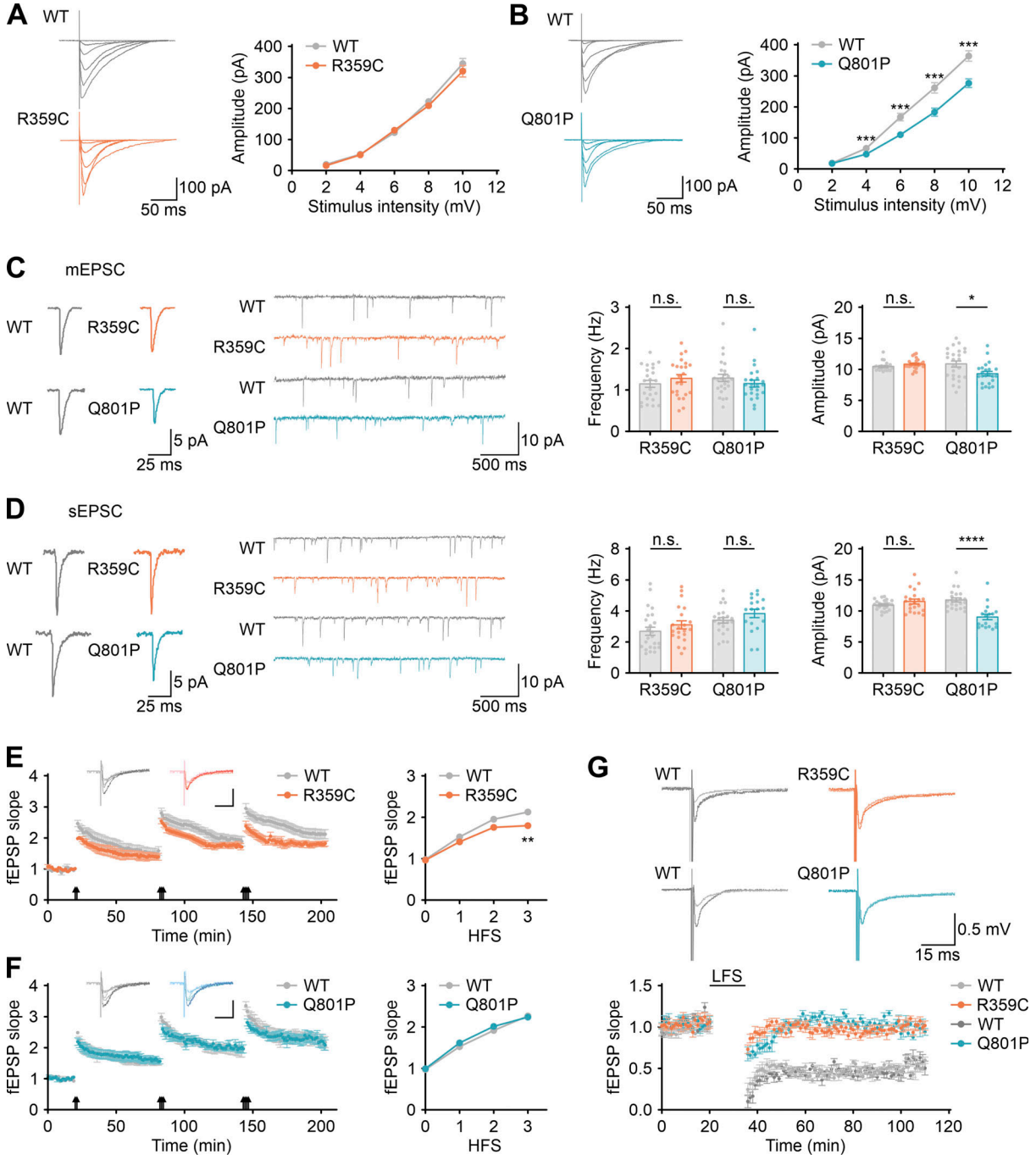

Figure 5. **Distinct synaptic phenotypes of the R359C and the Q801P mice. (A and B)** Representative recordings of the evoked EPSCs and plots showing the mean amplitudes (pA) of the EPSCs versus the stimulus intensities (mV) for CA1 pyramidal neurons in the slices from the R359C and Q801P mutant and their respective WT control littermates. Data are presented as mean ± SEM (n = 17–29 recordings per eight mice per group; ***P < 0.001; unpaired t test). **(C and D)** Representative traces and plots showing the frequency and the mean amplitude of the miniature and the spontaneous EPSCs recorded from CA1 pyramidal neurons from the R359C or Q801P mutant mice and their respective WT littermates. Data are presented as mean ± SEM (n = 18–25 recordings per eight mice per group; n.s., not significant; *P < 0.05; ****P < 0.0001; unpaired t test). **(E and F)** Plots showing the time course (left) and the summarized values 30 min after each tetanus (right) of the mean ± SEM (n = 15–24 recordings per five to eight mice per group; **P < 0.01; unpaired t test) of the 5–95% fEPSP slope, normalized to the baseline (defined as 1.0) immediately preceding first tetanus (↑) in the hippocampal slices from the R359C and Q801P mutant mice and their respective WT control littermates. Sample traces (inserts) show the baseline and sweeps at 15 min following tetani. Scale bars: 1 mV, 15 ms. **(G)** A plot showing the time course of the mean ± SEM (n = 15–25 recordings per five to eight mice per group) of the 5–95% fEPSP slope, normalized to the baseline (defined as 1.0) immediately preceding the low-frequency stimulation (LFS) in the hippocampal slices from the R359C and Q801P mutant mice and their respective WT littermates. Sample traces before and 30 min after LFS are shown at the top of the plot.

IQSEC2 R359C and Q801P mice show different impaired cognition patterns

Given the prevalence of cognitive impairments among patients carrying IQSEC2 variants (Shoubridge et al., 2010, 2019), it was incumbent upon us to explore potential cognitive deficiencies in our transgenic mouse models. We initiated this exploration through novel object recognition tasks (Fig. 6 A and Fig. S4 C). Remarkably, the R359C mutant mice displayed an equitable interest in both novel and familiar objects, diverging substantially from the WT mice, which clearly favored novel objects; this was reflected in the recognition indices (RIs) which registered 37.66% for WT and mere −1.07% for the R359C mice (Fig. 6 B). Surprisingly, while the Q801P mice also preferred novel objects versus the familiar ones (RI = 31.51%), they spent considerably less time exploring the objects (Fig. 6, A and B). Corroborating this, we noted that the Q801P mice spent significantly less time in the center area and made fewer entries into the center and object zones during both the initial habituation session and subsequent training and testing trials (Fig. S4, C–F), indicating potential alterations in exploratory and emotional behavior. This was further substantiated by our elevated plus maze tests, where Q801P mice showed decreased entries and time spent in the open arms of the maze as compared with the WT mice (Fig. 6 C). Interestingly, however, all test groups, including the R359C and Q801P mutants and their respective control littermates, performed normally in the sucrose preference, tail suspension, forced swim, acoustic startle response, and prepulse inhibition tests (Fig. S4, G–J).

Next, we examined the performance of the mice in the Morris water maze tests. In this test, the mice were trained to navigate to a hidden platform using visual cues. Intriguingly, our data showed that the R359C mice struggled more than their WT counterparts in navigating to a hidden platform using visual cues, with significantly longer escape latencies and swim path lengths throughout the training sessions (Fig. 6, D and E). After the training sessions, the mice were subjected to probe trials, in which the platform was removed on day 9. The R359C mice spent substantially less time in the target quadrant (Fig. 6 F), showing deficits in spatial learning and memory. The Q801P mice, however, performed similarly to the WT control littermates in both the training and the probe trials (Fig. 6, D–F). To assess the capacity of the mice to retrieve information learned and the flexibility to relearn new strategies, we performed the reversal training and the probe trials tests, in which the hidden platform was placed in the opposite quadrant (Fig. 6, D and E). Under this circumstance, the Q801P mutant exhibited minor defects in the reversal learning with significant impairments in memory retention/retrieval (Fig. 6 G). Nevertheless, in the visible platform version of the water maze test, all groups of mice performed equivalently (Fig. S4, K and L). Thus, the R359C mutation impairs both spatial learning and cognitive flexibility, whereas the Q801P mutation mainly affects the reversal of spatial learning and memory.

IQSEC2 R359C mice exhibit autistic behaviors

Patients carrying the p.R359C or p.Q801P variants of *Iqsec2* also exhibit autistic behaviors (Shoubridge et al., 2010, 2019). We, therefore, examined the social behaviors of the mutant mice by using the three-chamber social interaction tests (Fig. S4 M). In the habituation phase, all the groups of mice had no location preference for any chamber (Fig. S4 N). A remarkable decrease in social interactions was observed in the R359C mice as they showed no preference for stranger mice over novel objects (Fig. 6, H and I). Similar to the observation in the novel object recognition tasks, the Q801P mice displayed less motivation to explore both the object and mouse chambers (Fig. 6 H).

Conclusively, the R359C and Q801P mutations produced distinct behavioral and synaptic phenotypes. The R359C mice were impaired in activity-dependent synaptic plasticity (both LTP and LTD) expression, object recognition, spatial learning and memory, and social interactions. Conversely, the Q801P mice revealed deficits in basal synaptic transmission and LTD induction, exploration, and reversal learning. These findings provide substantial insights into the diverse behavioral and cognitive alterations linked to different IQSEC2 mutations, advancing our understanding of the complex pathological manifestations of these genetic variants.

Discussion

Iqsec2 has been established as a neurodevelopmental disability gene (Levy et al., 2019). Patients with IQSEC2 variants present a wide spectrum of clinical features, but the principal mechanisms responsible for IQSEC2-related disorders are still largely unknown. As a highly abundant ARF-GEF enriched in the central nervous system, particularly in the PSD, the functions and spatiotemporal regulation of the IQSEC2 GEF activity remained enigmatic. To address this knowledge gap, our study utilized an integrative approach combining biochemistry, structural biology, and in vivo models of transgenic mice, and elucidated a molecular model that depicts the autoinhibition and Ca^{2+}-dependent allosteric activation of IQSECs.

We discovered a novel GEF regulatory mechanism by solving the high-resolution apo-CaM/IQ/Sec7-PH ternary structure of IQSEC1. Unlike other ARF-GEFs that share commonalities in activity controls by impacting either the membrane recruitment or catalytic efficiency, the atypical PH domain of IQSECs has been reported to constitutively potentiate nucleotide exchange of the Sec7 domain (Aizel et al., 2013; Jian et al., 2012), leaving a question on how the temporal silencing and activation of IQSECs could be achieved. The atomic structures of the autoinhibited IQSECs together with detailed biochemical and enzymatic studies uncover a previously unrecognized and intricate Ca^{2+}-induced activity regulation mechanism of the ARF GEFs (Fig. 7). Under resting conditions in cells or synapses, the catalytic Sec7-PH tandem of IQSECs is very tightly inhibited by synergistic actions of the IQ-motif together with apo-CaM. The structures of apo-CaM-bound IQSECs also suggest that the negatively charged apo-CaM may block the autoinhibited enzymes from binding to plasma membranes via its PH domain and thus preventing the enzyme from engaging with membrane-anchored ARFs (Fig. 7). Future work is required to directly test the above hypothesis. Apo-CaM-bound IQSEC2 is likely enriched in the postsynaptic density via its C-terminal PDZ binding motif-mediated binding to synaptic scaffold proteins such as PSD-95 (Sakagami et al.,

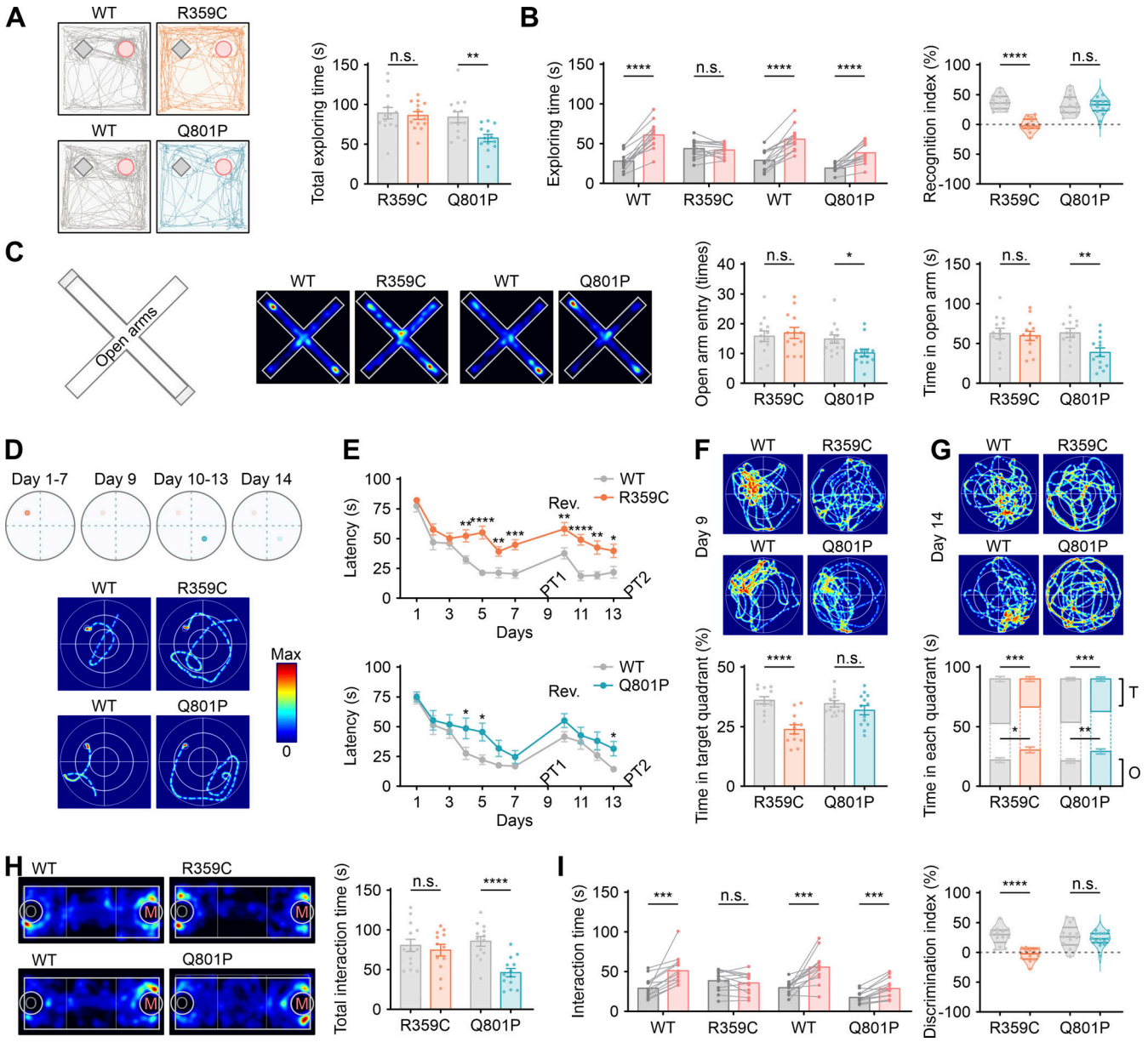

Figure 6. **Distinct behavioral phenotypes of the R359C and the Q801P mice. (A)** Representative exploration trajectories and the total time spent exploring both the familiar (diamond) and novel (circle) objects of the R359C and Q801P mutant mice and their respective WT control littermates in the novel object recognition task. Data are presented as mean ± SEM (n = 13 mice per group; n.s., not significant; **P < 0.01; unpaired t test). **(B)** Left: Bar graphs showing the time spent exploring the familiar (gray) and novel (red) objects during the test phase of the individual mice. Right: Relative preference for the novel object was calculated by a recognition index using violin plots. Data are presented as median, quartiles, and individual values (n = 13 mice per group; ****P < 0.0001; left: paired t test; right: unpaired t test). **(C)** Representative heatmaps and bar graphs showing the number of entrances and the time spent in the open arms of the elevated plus maze (EPM). Data are presented as mean ± SEM (n = 13 mice per group; *P < 0.05; **P < 0.01; unpaired t test). **(D)** Representative exploration trajectories on the seventh day during training in the Morris water maze test. Hidden platform positions presented each day are indicated above the graphs. Noted that the platform was removed in probe tests on the 9th and 14th days. **(E)** The escape latency during initial and reversal training in the Morris water maze to reach the hidden platform. Data are presented as mean ± SEM (n = 12–13 mice per group; *P < 0.05; **P < 0.01; ***P < 0.001; ****P < 0.0001; unpaired t test). **(F)** Representative exploration trajectories and quantification of time spent in the target quadrant in the first probe trial on the 9th day. Data are presented as mean ± SEM (n = 12–13 mice per group; ****P < 0.0001; unpaired t test). **(G)** Representative exploration trajectories and quantification of time spent in the original (O) and target (T) quadrants in the reversal probe trials on the 14th day. Data are presented as mean ± SEM (n = 12–13 mice per group; *P < 0.05; **P < 0.01; ***P < 0.001; unpaired t test). **(H)** Representative heatmaps and bar graphs show the time spent on exploring a novel object versus interacting with a stranger mouse. Data are presented as mean ± SEM (n = 12–13 mice per group; ****P < 0.0001; unpaired t test). **(I)** Left: Bar graphs showing the time spent exploring the novel object (O, gray) and stranger mouse (M, red) during the testing phase of individual mice. Right: Relative preference for the stranger mouse was calculated by a discrimination index showing by violin plots. Data are presented as median, quartiles, and individual values (n = 12–13 mice per group; ***P < 0.001; ****P < 0.0001; left: paired t test; right: unpaired t test).

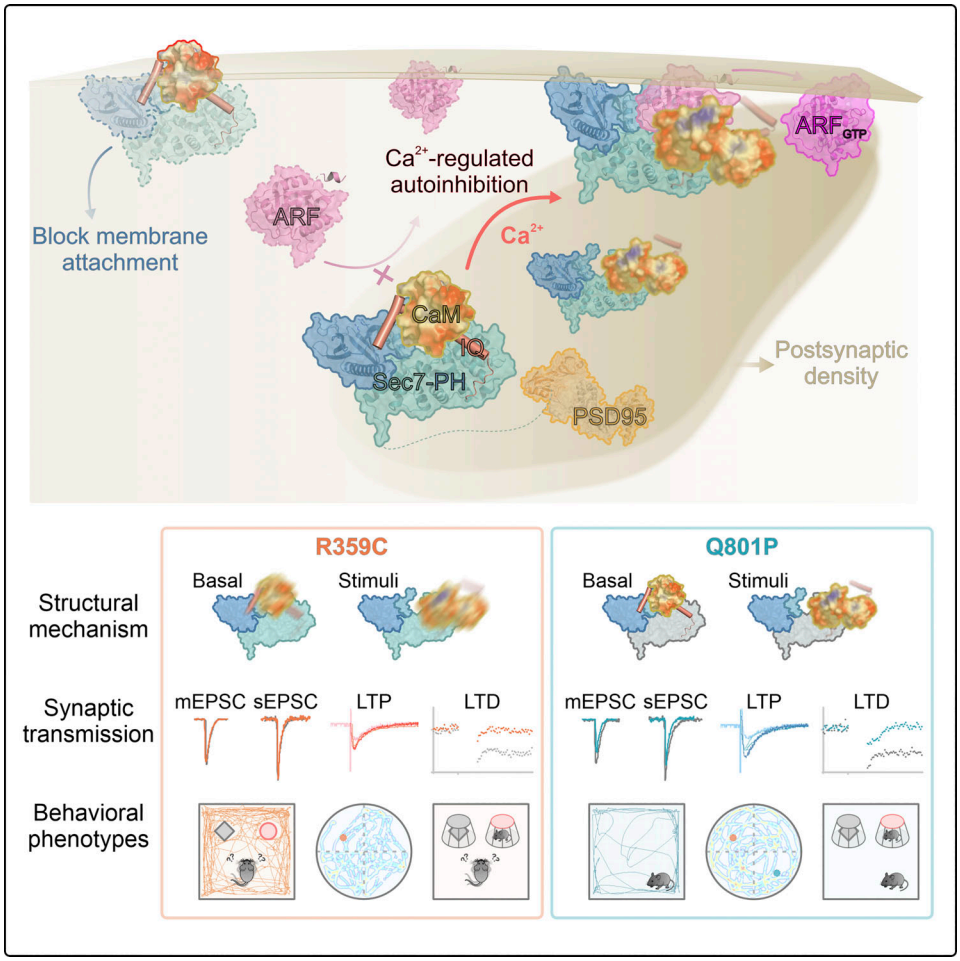

Figure 7. **Schematic model of Ca^{2+}-dependent IQSEC regulation.** IQSEC2 is likely enriched in synapses via its C-terminal PDZ binding motif-mediated binding to synaptic PDZ domain scaffold proteins such as PSD-95. The Apo-CaM-bound IQ-motif binds tightly to the Sec7-PH tandem, blocking ARFs from accessing the catalytic core. The IQSEC-bound negatively charged Apo-CaM occludes the PH domain from binding to lipid membranes. The rise of cellular Ca^{2+} concentration releases the autoinhibition and concomitantly allows the enzyme to bind to lipid membranes and membrane-localized ARFs, resulting in a synergistic production of GTP-bound ARFs.

2008). When cells or synapses are activated, the influx of Ca^{2+} releases the autoinhibited conformation of the enzyme by lifting the elongated IQ-motif from the active site of the enzyme and concomitantly allowing the Sec7-PH tandem to be able to bind to lipid membranes and ARFs localized at lipid membranes, leading to highly synergistic activation of the enzyme triggered by Ca^{2+} (Aizel et al., 2013; Jian et al., 2012; Karandur et al., 2017; Nawrotek et al., 2019). It is worth noting that the high-affinity binding of Ca^{2+}-CaM to the IQ-motif keeps CaM associated with IQSECs even at elevated Ca^{2+} concentrations. Our in vitro GEF assays showed that IQSEC2 without CaM bound exists in an intermediate state between the apo-CaM bound, fully auto-inhibited state, and the Ca^{2+}-CaM bound, fully activated state (Fig. 4 E). Nonetheless, given CaM is highly abundant in synapses, such intermediate state may not be functionally relevant. The continued binding of Ca^{2+}-CaM to activated IQSEC2 primes the enzyme to be able to rapidly respond to cellular/synaptic Ca^{2+} concentration changes. For example, the activity of IQSECs can be rapidly inactivated when synaptic Ca^{2+} concentration returns to the basal level after synaptic stimulation.

Our electrophysiological study using acute hippocampal slices from transgenic mice carrying two different pathogenic variants, R359C in the IQ-motif and Q801P in the Sec7 domain of IQSEC2, demonstrated that the Ca^{2+}-dependent activation of IQSEC2 is essential for synaptic plasticity, especially the LTD of synaptic transmissions. Interestingly, the Q801P and R359C mutations, while both resulting in impaired LTD induction, affect IQSEC2 functions through distinct mechanisms. The Q801P mutation, which leads to impaired GEF activity of IQSEC2, was found to be defective in LTD induction in mice, suggesting that the GEF activity of IQSEC2 is required for synaptic AMPAR removal. Conversely, the R359C mutation, which has an increased GEF activity at the basal condition but loses its Ca^{2+}-induced activity enhancement, also displays impaired LTD induction in mice. Based on the available data, it appears probable that the R359C mutant is unable to facilitate LFS-induced synaptic AMPAR removal due to its inability to enhance GEF activity in response to Ca^{2+} (i.e., the GEF activity of the mutant IQSEC2 is saturated already). Interestingly, the R359C mice also exhibited abnormally quick ceiling effects in LTP, which may arise from

the impaired Ca^{2+} sensitivity of IQSEC2. Further studies on Ca^{2+}-dependent modulation of IQSEC2 are needed to tease out the details of mutation-induced synaptic functional defects.

These electrophysiological findings underscore the nuanced influence of different pathogenic IQSEC2 mutations on synaptic plasticity and transmission, reasoning the partially overlapping but largely distinct pathological behavior phenotypes observed in two transgenic mice models. Both R359C and Q801P mice displayed impaired learning abilities, mirroring ID symptoms found in patients carrying the mutations. Additionally, the R359C mice showed repetitive behavior and impaired social interactions, characteristics typically observed in autism patients, whereas the Q801P mice displayed anxiety-like phenotypes, such as lacking motivation in exploration. The unique mechanisms by which these two mutations affect IQSEC2's activity and function offer explanations for the puzzling observation of these phenotypes and reaffirm the necessity for personalized therapeutic strategies for patients with different IQSEC2 mutations. By comprehensively understanding the link between specific mutations, synaptic transmission alterations, and associated behavioral changes, our study starts to pave the way for devising effective strategies for treating *Iqsec2* mutation-related disorders.

Materials and methods

Plasmid constructs

The full-length cDNAs encoding human IQSEC1 (GenBank ID NM_001134382), IQSEC2 (NM_001111125), and IQSEC3 (NM_001170738) were synthesized by YouBio. The expression plasmid of rat IQSEC3 (NM_207617) was a gift from Dr. Ji Won Um at Daegu Gyeongbuk Institute of Science and Technology, Daegu, Korea. The coding sequence of mouse ARF1 (NM_001130408) was amplified from a mouse cDNA library. All truncations and mutations used in this study were generated by the standard PCR-based methods. For protein purification, PCR products were inserted into pGEX 4T-1 or modified pET vectors with an N-terminal His_6- or TRX-His_6-tag followed by an HRV-3C protease cutting site (pET.M3C/pET.32M3C). Constructs encoding the IQ-motif were cloned into pET.32M3C vectors together with human CaM (NM_005184) for coexpression. For protein expression in heterologous cells, PCR products were cloned into modified pEGFP-C3 vectors. All constructs were verified by DNA sequencing.

Purification of recombinant proteins from *E. coli*

Recombinant proteins were expressed in *E. coli* BL21 (DE3) cells (Agilent Technologies) in LB medium at 16°C for 16–20 h after IPTG induction. Protein purification was performed using Ni^{2+}-NTA agarose affinity column (for His_6-tag proteins) or GSH-Sepharose affinity column (for GST-tag proteins) followed by size-exclusion chromatography (SEC) with a column buffer containing 50 mM Tris pH 8.2, 100–500 mM NaCl, 1 mM EDTA, and 1 mM DTT. His_6-/TRX-His_6-tags were cleaved by HRV-3C protease at 4°C overnight and removed by another step of SEC or ion-exchange chromatography. For measurements of protein–protein interactions or structure determination, purified proteins were assayed in a buffer containing 50 mM Tris pH 8.2, 100 mM NaCl, and 1 mM DTT with the indicated concentration of EDTA or $CaCl_2$. For nucleotide exchange assays, purified proteins were finally exchanged into an assay buffer containing 25 mM HEPES pH 7.4, 100 mM NaCl, 1 mM $MgCl_2$, and 1 mM DTT with 1 mM EGTA or 1 mM $CaCl_2$.

Isothermal titration calorimetry (ITC)

ITC measurements were performed using a MicroCal VP-ITC calorimeter (Malvern). The experiment took place at 25°C (or 10°C in certain cases) in the assay buffer with 10–20 μM of each indicated protein in the sample cell titrated with its binder at 100–200 μM. Each titration point contained an injection of 10 μl aliquot delivered in 20 s with a 120-s interval between successive injections. Data were analyzed using the simple single-site binding model by the Origin 7 software.

Size-exclusion chromatography coupled to multi-angle light scattering (SEC-MALS)

SEC-MALS assay was performed on an AKTA purifier system (GE Healthcare) coupled with a static light scattering detector (miniDawn, Wyatt) and a differential refractive index detector (Optilab, Wyatt). Typically, 100 μl of purified protein or mixture at an 80–100 μM concentration was loaded to a Superose 12 10/300 GL column in a column buffer composed of 50 mM Tris pH 8.2, 100 mM NaCl, and 1 mM DTT with 1 mM EDTA or 5 mM $CaCl_2$. Data were analyzed using ASTRA6 (Wyatt).

Crystallization and structure determination

Crystals of IQSEC1 apo-CaM/IQ/Sec7-PH complex were obtained by sitting drop vapor-diffusion method at 16°C. Purified Sec7-PH (aa 517–882) protein and IQ (aa 106–173)/apo-CaM (aa 1–148) complex were mixed at a molar ratio of 1:1.5 with the concentration of 2.5 mg/ml in a buffer containing 50 mM Tris pH 8.2, 100 mM NaCl, 1 mM DTT, and 1 mM EDTA. The complex solution was mixed with equal volume (1 + 1 μl) of the reservoir buffer containing 0.1 M HEPES pH 7.5 and 4% wt/vol polyethylene glycol 8,000 for crystallization. Crystals were cryoprotected with 20% (vol/vol) glycerol and flash-cooled to 100 K.

X-ray diffraction data were collected at the BL17U or BL19U1 beamlines at the Shanghai Synchrotron Radiation Facility (SSRF). Diffraction data were processed using HKL2000 or HKL3000 (Otwinowski and Minor, 1997). The structure was solved by molecular replacement method by Phaser (McCoy et al., 2007) using the structure of IQSEC1 Δ17ARF1-GDP/Sec7-PH complex (PDB code: 4C0A) as the searching model. Manual model building and refinement were carried out iteratively using Coot (Emsley et al., 2010) and PHENIX (Adams et al., 2010). The final models were validated by MolProbity (Chen et al., 2010), and statistics are summarized in Table S1. All structure figures were drawn using PyMOL (http://www.pymol.org).

NMR spectroscopy

NMR samples contained 300–500 μM ^{15}N-labeled proteins in 50 mM Tris pH 8.2, 100 mM NaCl, 1 mM DTT with 1 mM EDTA, or 1 mM $CaCl_2$ in 90% H_2O/10% D_2O. HSQC spectrum was acquired at 30°C on Varian Inova 800-MHz spectrometers

equipped with an actively z-gradient-shielded triple resonance probe. Backbone resonance assignments of CaM were obtained from a previous paper (Mal and Ikura, 2008).

Fluorescent-based nucleotide exchange assays

Bacterially purified N terminal–truncated Δ17ARF1 was assayed in nucleotide exchange reactions. Δ17ARF1 was preloaded with GDP in the presence of EDTA before reactions and excess nucleotides were removed by SEC. Upon nucleotide exchange, the conversion of ARF1-GDP to ARF1-mantGTP resulted in fluorescence resonance energy transfer (FRET) from intrinsic fluorescence of tryptophan in ARF1 (excitation, 297 nm; emission, 340 nm) to the methyl anthro noyl group on mantGTP (excitation, 350 nm; emission, 450 nm; Fig. 3 B).

Nucleotide exchange kinetics were measured by fluorescence spectroscopic analysis of mantGTP incorporation signal (excitation, 297 nm; emission, 450 nm) using a FlexStation 3 multimode microplate reader (Molecular Devices). 20 μM (final) Δ17ARF1-GDP was rapidly mixed with mixtures containing 20 μM (final) mantGTP and indicated concentrations of IQSEC proteins in the assay buffer (25 mM HEPES pH 7.4, 100 mM NaCl, 1 mM $MgCl_2$, 1 mM DTT with 1 mM EGTA or 1 mM $CaCl_2$) to initiate the reaction. The fluorescence measurements were carried out every 10 s for a total time of 60 min at 30°C.

The kinetic traces were fitted with a one-phase exponential association model to determine k_{obs} values, and k_{cat}/K_M values were calculated by linear regression from plots of k_{obs} against a range of GEF protein concentrations following the Michaelis–Menten equation. All measurements were repeated four times. Data were analyzed using GraphPad Prism.

GST pull-down assay

Plasmids encoding GFP-tagged IQ-motif of IQSEC2 (aa 300–395) or its mutants were transiently transfected into HEK293T cells using Lipofectamine and Plus reagents (Thermo Fisher Scientific). The cells were harvested at 18–20 h after transfection and lysed on ice for 30 min using the lysis buffer containing 50 mM Tris pH 7.5, 150 mM NaCl, 10% glycerol, 1% Triton X-100, 2 mM DTT, and a cocktail of protease inhibitors (Merck). After centrifugation, 0.1 ml supernatant was incubated with 2 μM (final) GST-tagged CaM in 1 ml (final) reaction buffer containing 50 mM Tris pH 7.5, 150 mM NaCl with 2 mM EGTA, or 2 mM $CaCl_2$ (Triton X-100 was diluted to 0.1%). The mixture was incubated with rotation at 4°C for 30 min and then 25 μl fresh GSH Sepharose resin was added and incubated again for another 30 min. After extensive washing with corresponding wash buffer (50 mM Tris pH 7.5, 150 mM NaCl, 0.1% Tween 20 with 2 mM EGTA or 2 mM $CaCl_2$), the captured proteins were eluted by the sample loading dye buffer and analyzed by Western blot.

Animals

All experimental procedures were conducted following protocols approved by the Institutional Animal Care and Use Committee (IACUC) of the animal core facility at Huazhong University of Science and Technology, Wuhan, China. Mice were housed in groups of three to five mice/cage under a 12-h light-dark cycle (lighting from 8:00 to 20:00) with food and water ad libitum, at a consistent ambient temperature (21 ± 1°C) and humidity (50 ± 5%). All tests were performed during the light phase. The mice were handled daily by experimenters for at least 3 d and were then transferred to the testing room for 1-h acclimation before starting the experiments, as described before (He et al., 2022; Li et al., 2022). Hemizygous and WT littermate males of the single line generated by heterozygous breeding were used as mutant and control mice, respectively, throughout this study. And mice were randomly allocated to different experimental groups. All behaviors were scored by experimenters who were blinded to genotypes.

Generation of IQSEC2 mutant mice

The N-terminal mScarlet-tagged *Iqsec2* knock-in mice were generated in the present study through sperm-like stem cell-mediated semicloning technology (Yang et al., 2012a; Zhong et al., 2015). IQSEC2 R359C and Q801P mice were generated by the CRISPR-Cas9-mediated extreme genome editing system (Beijing Biocytogen). Cas9-guide RNA (gRNA) target sequences were designed to the regions on exon 3–4 or 5–6 to promote DNA breaks and homologous recombination, respectively. The in vitro-transcribed Cas9 mRNA, gRNA, and the oligo donors carrying the desired mutation (*p.R359C*, *c.C1075T*, *A1077C*, or *p.Q801P*, *c.A2402C*) were coinjected into fertilized mouse eggs. Primers used for genotyping were as follows: *Iqsec2* R359C-F: 5′-AGCCTG TCATGACTTCCAGCAGTT-3′; R359C-R: 5′-TAAGGGAGGCCC CGTTCAAGC-3′; Q801P-F: 5′-GACCAGGCACAGTTCTAGAGG AACA-3′; Q801P-R: 5′-AATAAGACCCTTTTGGAGCAGAGGG-3′.

Brain weight and histochemistry

Male mice at 90 ± 3 d old were sacrificed by intraperitoneal injection of an overdose of pentobarbital sodium and were transcranial-perfused with 100 ml of saline (0.9% wt/vol NaCl) followed by 4% PFA. Whole brains were dissected and post-fixed in 4% PFA for 24 h. Brains from four individual groups were weighed. Coronal brain sections (30 μm) were collected at −20°C with a cryostat (Leica Microsystems). Free-floating coronal sections were rinsed in PBS three times and then incubated in 50 mM Tris-HCl buffer containing DAPI for 10 min. Sections were rinsed, dried, and mounted with Antifade Mountant (P36961; Invitrogen). Images were acquired with a confocal laser-scanning microscope (Zeiss LSM800 Examiner Z1) and an automated slide-scanning microscope (Olympus VS120).

Electrophysiology

Male mice aged 60 ± 2 d and 21–25 d (for LTP and LTD, respectively) were shortly anesthetized with isoflurane and decapitated. The brains were rapidly removed and the hippocampal slices were immediately prepared in ice-cold slicing artificial cerebrospinal fluid (ACSF; in mM: 120 choline chloride, 26 $NaHCO_3$, 25 *D*-glucose, 5 Na-ascorbate, 7 $MgCl_2$, 3 Na-pyruvate, 2.5 KCl, 1.25 NaH_2PO_4, and 0.5 $CaCl_2$ at pH 7.4, with osmolarity at 305 mOsm) saturated with 95% O_2/5% CO_2. 300-μm-thick coronal sections were then transferred to a recovery chamber filled with recording ACSF (in mM: 124 NaCl, 3 KCl, 26 $NaHCO_3$, 1.2 $MgCl_2$, 1.25 $NaH_2PO_4 2H_2O$, 10 $C_6H_{12}O_6$, and 2 $CaCl_2$

at pH 7.4, 95% O_2/5% CO_2, 305 mOsm) and incubated at 32°C for 30 min, followed by 22°C for 60 min. A slice was transferred to a recording chamber, which was continuously perfused with oxygenated ACSF (2 ml/min) at 22°C, as described before (He et al., 2022; Li et al., 2021, 2022).

For whole-cell patch-clamp recordings from the CA1 pyramidal cells, hippocampal slices were visualized via input resistance-DIC by using an Axioskop 2FS equipped with Hamamatsu C2400-07E optics. Resting membrane potentials were measured immediately after the breakthrough. Basic electrophysiological properties were recorded when stable recordings were achieved with good access resistance (~20 MΩ). The EPSCs were evoked by bipolar tungsten electrodes, recorded with Axopatch 200B amplifiers, and monitored by computer using pClamp11 at 31.5°C in the presence of 10 μM bicuculline. Responses in CA1 pyramidal neurons were evoked by stimulation of the Schaffer-collateral fibers with the stimulus intensity from 4 to 10 mV at the interval of 2 mV. The spontaneous EPSCs (sEPSC) were recorded using an internal solution containing 140 mM potassium gluconate, 10 mM HEPES, 2 mM NaCl, 0.2 mM EGTA, 2 mM Mg^{2+}ATP, 0.3 mM NaGTP, and an external solution containing 10 μM bicuculline. The spontaneous inhibitory postsynaptic currents (sIPSC) were recorded using an internal solution containing 153.3 mM CsCl, 10 mM HEPES, 1 mM $MgCl_2$, 5 mM EGTA, 4 mM Mg^{2+}ATP, and an external solution containing 20 μM 6-cyano-7-nitroquinoxaline-2,3-dione (CNQX) and 50 μM APV. The miniature excitatory versus inhibitory postsynaptic currents (mEPSC/mIPSC) were recorded at the same condition as sEPSC/sIPSC with an additional presence of 1 μM tetrodotoxin (TTX). The row electrophysiological data were collected at 10 kHz, filtered with a low-pass filter at 2 kHz, and analyzed using ClampFit 10.2 software (Molecular Devices) with template matching at a threshold of 5 pA.

The standard extracellular recording was used to monitor field excitatory postsynaptic potentials (EPSPs) in the stratum radiatum of the CA1 area of the hippocampal slices in response to the Schaffer-collateral afferent stimulation. Both recording and stimulating electrodes were glass patch electrodes filled with ACSF and with a resistance of 3–5 MΩ. Recordings were made with an Axoclamp 2B amplifier (Molecular Devices) and signals were further processed (100× amplification, 5 kHz low pass filter) using a Brownlee model 440 signal processor (Brownlee Inc.). Data were monitored online and EPSP slopes were measured by taking the slope of the rising phase between 5% and 95% and analyzed off-line using Win LTP software, as described before (Li et al., 2022). EPSPs were evoked at a frequency of 0.1 Hz. After 10 min baseline, LTP saturation was induced by three tetani; the first tetanus consisted of two trains of 100 Hz stimulation lasting 500 ms at an intertrain interval of 10 s, the second tetanus consisted of three trains, and the third one consisted of four trains. Stimulation intensity at the baseline was set to ~35% of the maximal synaptic response. LTD was induced by a classical LFS (1 Hz, 900 pulses). LTD was measured 15 min after LFS. Data were gathered from recordings made from one to three slices per mouse brain and expressed as mean ± SEM of all the slices.

Behavioral analyses

Home cage behaviors

Individual male mice at 120 ± 5 d of age were tracked by video and infrared beam interruption alone in PhenoTyper home cages (40 × 40 × 40 cm; Noldus) with sufficient food and water supply. After 24-h habituation, locomotion and spontaneous behaviors were automatically analyzed by EthoVisionXT (Noldus) over 48 h.

Novel object recognition test

After acclimation, male mice at 120 ± 5 d old of age were placed facing the wall of an open-field arena (50 × 50 × 38 cm) and allowed to explore for 5-min habituation. In the training session, the mice were exposed to two identical objects placed near corners of the arena (3 cm from each adjacent wall) and again allowed to explore the arena for 5 min. Following a delay period of 1 h, mice underwent a 5-min test session in which two objects were placed in the same positions as in the training session but one was replaced by a novel object. The object type and position of the novel object were counterbalanced through all experiments to avoid bias. Explorative behavior was defined as a mouse approaching its nose pointed at a maximum distance of 2.5 cm from the object. The recognition discrimination index was defined as (T2 − T1)/(T1 + T2), where T1 = time spent exploring the familiar object and T2 = time spent exploring the novel object.

Elevated plus maze test

The apparatus used for the elevated plus maze test is 50 cm above the floor, comprising two open arms (28 × 6 cm, with 0.5 cm tall/wide ledges) across from each other and perpendicular to two closed arms (28 × 6 cm, with 15 × 0.5 cm tall/wide walls) with a center platform (6 × 6 cm). A mouse was placed in the center area of the maze with its head directed toward an open arm and allowed to move freely in the maze for 10 min. The number of entries (an entry is defined as the center of mass of the mouse entering the arm) into each arm and the time spent in the open arms were analyzed and served as an index of anxiety-like behaviors, as described before (He et al., 2022; Li et al., 2021, 2022).

Sucrose preference test

A 1% (wt/vol) fresh sucrose solution was prepared before the experiment each day. Each mouse was presented with two drinking bottles, one containing 1% sucrose and the other containing regular water, in their home cages for 24 h. The position of the two bottles was counterbalanced among groups to avoid side preference. The weight of the two bottles were recorded before and after the experiment. The sucrose preference was defined as sucrose solution consumption/(sucrose solution consumption + water consumption) × 100%.

Tail suspension test

A specially manufactured tail suspension box was made of white plastic with dimensions (50 height × 30 width × 25 cm depth) in which a suspended mouse could not make contact with the walls. A suspension bar with a diameter of 1 cm was fixed on the

top. The mouse's tail was stuck by tape in the middle of the bar. Behaviors of each mouse were recorded for 7 min and the immobility time of the last 5 min was analyzed.

Forced swim test

The swim cylinder (20 cm in diameter) was filled to 18 cm from the bottom with water at 23–25°C and space was left at the top for 10 cm so that mice could not escape. Mice were gently placed in the water and when mice floated without swimming to keep their heads above the water, they were judged to be immobile. Mouse behaviors were recorded for 7 min and the immobility time of the last 5 min was analyzed.

Acoustic startle response and prepulse inhibition tests

SR-LAB-Startle Response System was used to measure the acoustic startle response (ASR) to loud noise and prepulse inhibition (PPI) of the startle response. The response intensity was computed by SR-LAB Software. ASR was defined as the average response intensity of 28 times the startle stimulus. PPI was calculated as the following formula: %PPI = (1-startle response for pre-pulse with startle stimulus trial/startle response for startle stimulus without startle stimulus trial) × 100%.

Morris water maze

The water maze pool (120 cm in diameter; Chengdu TaiMeng Technology) was filled with water at 23–25°C and an escape platform (6 cm in diameter) was submerged 1 cm below the surface of the water during training. Titanium dioxide was dissolved in the water to obscure the platform. Four different graphic patterns were marked on the wall to offer navigation cues for mice to locate the hidden platform. The training session lasted for 7 d. On the first day of training, mice were allowed to rest on the platform for 30 s and had 90 s to find the hidden platform. In case a mouse did not find the platform within 90 s, it was guided to find and stay on the platform for 30 s. Each mouse was trained four times daily with 60-min intervals between successive training sessions, in which the mouse was released from randomized release points in four quadrants of the pool. After a 1-d interval, the platform was removed for probe tests and mice were placed into the pool in the quadrant opposite to the platform location and allowed to swim for 90 s. During the retrieval session, the hidden platform was shifted to the opposite quadrant of the original position. Mice were trained for another 4 d and probe tests were performed. The exploration trajectories were recorded. The latencies to reach the platform during training sessions and time spent in the original/target quadrant during probe trials were analyzed, as described before (He et al., 2022; Li et al., 2021, 2022).

Three-chamber sociability test

The three-chamber apparatus was made of white plastic with dimensions of 102 length × 47 width × 45 cm height. Two transparent side-crossing walls are left with a width of 10 cm allowing mice to cross freely. The cup-like containers (10 cm in diameter × 12 cm in height) were comprised of metal wires with 1-cm gaps to allow for air exchange but small enough to prevent direct physical interactions. A cone-type object made of the same material was placed on the top of the cup to prevent the test mouse from climbing. In the habituation session, mice were placed in the middle of the apparatus with two empty containers on each side and allowed to explore for 10 min. Following a delay period of 1 h, mice underwent a 10-min test session in which an age-, sex-, and strain-matched unfamiliar WT mouse was placed in one of the containers to serve as the social stimulus, while a novel object was placed in another container. The positioning of containers was counterbalanced throughout all experiments to avoid bias. Exploring time on each side of the apparatus during the habituation session was recorded. In the test session, interaction behavior was defined as a mouse approaching its nose within 1 cm of the container. The social preference discrimination index was calculated as (M − O)/(M + O), where M indicates the time spent interacting with the unfamiliar mouse and O represents the time spent exploring the novel object, as described before (He et al., 2022; Li et al., 2022; Yang et al., 2012b).

Quantification and statistical analysis

All electrophysiology and animal behavior values in the text and figure legends are represented as the mean ± SEM. Unpaired or paired two-tailed Student's *t* tests (*t* test) were used when assumptions of normality and equal variance (*F* test) were met. Significance was accepted for $P < 0.05$. Power calculations were performed using GraphPad Prism v9.0. Group sizes were estimated based on previous studies (He et al., 2022; Li et al., 2021, 2022; Yang et al., 2012b). All statistical data are summarized in Table S1.

Online supplemental material

Fig. S1 shows that the IQ-motif/CaM complex is also coupled with the Sec7-PH tandem and dissociated by Ca^{2+} in IQSEC1 and IQSEC2. Fig. S2 shows the comparisons of the Apo-CaM/IQ/Sec7-PH ternary structure with those of related proteins. Fig. S3 shows the generation and characterization processes of *mScarlet-Iqsec2*, IQSEC2 R359C, and IQSEC2 Q801P mice. Fig. S4 shows behavioral phenotypes of the R359C and the Q801P mice. Table S1 summarizes the statistical data.

Data availability

The atomic coordinates of IQSEC1-IQ motif, Sec7PH tandem in complex with CaM can be accessed at the Protein Data Bank (PDB) with the accession number 7VMB.

Acknowledgments

We thank the BL19U1 and BL17U1 beamlines at the National Facility for Protein Science Shanghai (NFPS) for the X-ray beam time.

This work was supported by grants from National Natural Science Foundation of China (82188101), the Minister of Science and Technology of China (2019YFA0508402), Shenzhen Bay Laboratory (S201101002), Shenzhen Talent Program (KQTD20210811090115021), Shenzhen Science and Technology Basic Research Program (JCYJ20220818100215033), Guangdong Innovative and Entrepreneurial Research Team Program (2021ZT09Y104), Research Grants Council of Hong Kong

(16104518 and 16101419), and the Human Frontier Science Program Research Grant (RGP0020/2019) to M. Zhang; National Natural Science Foundation of China (grants: 31721002 to Y. Lu; 81920208014 to Y. Lu; 31930051 to Y. Lu; 32200795 to H. Li); Natural Science Foundation of Hubei Province (2022CFB608) to H. Li. G. Bai is supported by the President's Excellent Postdoctoral Program of SUSTech.

Author contributions: G. Bai, H. Li, Y. Lu, and M. Zhang conceived the idea and designed the experiments; G. Bai performed all biochemical experiments and data analysis; W. Yang and G. Bai solved the structures; M. Wu and R. Huang prepared samples; H. Li, P. Qin, and Y. Lu generated the mutant mice, performed the mice genotyping, PCR, histochemical and the behavioral studies; H. Li and Y. Guo performed electrophysiological recordings; F. Ye carried out NMR studies; J. Chen and J. Li generated the mScarlet-tagged IQSEC2 mice; G. Bai, H. Li, Y. Lu, and M. Zhang wrote and revised the manuscript, and all authors provided input, M. Zhang coordinated the study.

Disclosures: The authors declare no competing interests exist.

Submitted: 24 July 2023
Revised: 31 August 2023
Accepted: 14 September 2023

References

Accogli, A., G. Eric Jarvis, A. Schiavetto, L. Lai, E.L. Amirali, D.A. Jimenez Cruz, J.B. Rivière, and Y. Trakadis. 2020. Psychiatric features and variable neurodevelopment outcome in four females with IQSEC2 spectrum disorder. *J. Genet.* 99:47.

Adams, P.D., P.V. Afonine, G. Bunkóczi, V.B. Chen, I.W. Davis, N. Echols, J.J. Headd, L.W. Hung, G.J. Kapral, R.W. Grosse-Kunstleve, et al. 2010. PHENIX: A comprehensive python-based system for macromolecular structure solution. *Acta Crystallogr. D Biol. Crystallogr.* 66:213–221. https://doi.org/10.1107/S0907444909052925

Aizel, K., V. Biou, J. Navaza, L.V. Duarte, V. Campanacci, J. Cherfils, and M. Zeghouf. 2013. Integrated conformational and lipid-sensing regulation of endosomal ArfGEF BRAG2. *PLoS Biol.* 11:e1001652. https://doi.org/10.1371/journal.pbio.1001652

Ansar, M., H.L. Chung, A. Al-Otaibi, M.N. Elagabani, T.A. Ravenscroft, S.A. Paracha, R. Scholz, T. Abdel Magid, M.T. Sarwar, S.F. Shah, et al. 2019. Bi-allelic variants in IQSEC1 cause intellectual disability, developmental delay, and short stature. *Am. J. Hum. Genet.* 105:907–920. https://doi.org/10.1016/j.ajhg.2019.09.013

Bähler, M., and A. Rhoads. 2002. Calmodulin signaling via the IQ motif. *FEBS Lett.* 513:107–113. https://doi.org/10.1016/S0014-5793(01)03239-2

Barrie, E.S., C.E. Cottrell, J. Gastier-Foster, S.E. Hickey, A.D. Patel, S.L. Santoro, and M.P. Alfaro. 2020. Genotype-phenotype correlation: Inheritance and variant-type infer pathogenicity in IQSEC2 gene. *Eur. J. Med. Genet.* 63:103735. https://doi.org/10.1016/j.ejmg.2019.103735

Brown, J.C., A. Petersen, L. Zhong, M.L. Himelright, J.A. Murphy, R.S. Walikonis, and N.Z. Gerges. 2016. Bidirectional regulation of synaptic transmission by BRAG1/IQSEC2 and its requirement in long-term depression. *Nat. Commun.* 7:11080. https://doi.org/10.1038/ncomms11080

Chen, V.B., W.B. Arendall III, J.J. Headd, D.A. Keedy, R.M. Immormino, G.J. Kapral, L.W. Murray, J.S. Richardson, and D.C. Richardson. 2010. MolProbity: All-atom structure validation for macromolecular crystallography. *Acta Crystallogr. D Biol. Crystallogr.* 66:12–21. https://doi.org/10.1107/S0907444909042073

Emsley, P., B. Lohkamp, W.G. Scott, and K. Cowtan. 2010. Features and development of Coot. *Acta Crystallogr. D Biol. Crystallogr.* 66:486–501. https://doi.org/10.1107/S0907444910007493

He, A., C. Zhang, X. Ke, Y. Yi, Q. Yu, T. Zhang, H. Yu, H. Du, H. Li, Q. Tian, et al. 2022. VGLUT3 neurons in median raphe control the efficacy of spatial memory retrieval via ETV4 regulation of VGLUT3 transcription. *Sci. China Life Sci.* 65:1590–1607. https://doi.org/10.1007/s11427-021-2047-8

Jian, X., J.M. Gruschus, E. Sztul, and P.A. Randazzo. 2012. The pleckstrin homology (PH) domain of the Arf exchange factor Brag2 is an allosteric binding site. *J. Biol. Chem.* 287:24273–24283. https://doi.org/10.1074/jbc.M112.368084

Karandur, D., A. Nawrotek, J. Kuriyan, and J. Cherfils. 2017. Multiple interactions between an Arf/GEF complex and charged lipids determine activation kinetics on the membrane. *Proc. Natl. Acad. Sci. USA.* 114:11416–11421. https://doi.org/10.1073/pnas.1707970114

Karplus, P.A., and K. Diederichs. 2012. Linking crystallographic model and data quality. *Science.* 336:1030–1033. https://doi.org/10.1126/science.1218231

Levy, N.S., V. Borisov, O. Lache, and A.P. Levy. 2023. Molecular insights into IQSEC2 disease. *Int. J. Mol. Sci.* 24:4984. https://doi.org/10.3390/ijms24054984

Levy, N.S., G.K.E. Umanah, E.J. Rogers, R. Jada, O. Lache, and A.P. Levy. 2019. IQSEC2-associated intellectual disability and autism. *Int. J. Mol. Sci.* 20:3038. https://doi.org/10.3390/ijms20123038

Li, J., Y. Chen, Y. Deng, I.C. Unarta, Q. Lu, X. Huang, and M. Zhang. 2017. Ca^{2+}-induced rigidity change of the myosin VIIa IQ motif-single α helix lever arm extension. *Structure.* 25:579–591.e4. https://doi.org/10.1016/j.str.2017.02.002

Li, X., W. Chen, X. Huang, W. Jing, T. Zhang, Q. Yu, H. Yu, H. Li, Q. Tian, Y. Ding, and Y. Lu. 2021. Synaptic dysfunction of Aldh1a1 neurons in the ventral tegmental area causes impulsive behaviors. *Mol. Neurodegener.* 16:73. https://doi.org/10.1186/s13024-021-00494-9

Li, X., H. Yu, B. Zhang, L. Li, W. Chen, Q. Yu, X. Huang, X. Ke, Y. Wang, W. Jing, et al. 2022. Molecularly defined and functionally distinct cholinergic subnetworks. *Neuron.* 110:3774–3788.e7. https://doi.org/10.1016/j.neuron.2022.08.025

Lopergolo, D., F. Privitera, G. Castello, C. Lo Rizzo, M.A. Mencarelli, A.M. Pinto, F. Ariani, A. Currò, V. Lamacchia, R. Canitano, et al. 2021. IQSEC2 disorder: A new disease entity or a rett spectrum continuum? *Clin. Genet.* 99:462–474. https://doi.org/10.1111/cge.13908

Lowenthal, M.S., S.P. Markey, and A. Dosemeci. 2015. Quantitative mass spectrometry measurements reveal stoichiometry of principal postsynaptic density proteins. *J. Proteome Res.* 14:2528–2538. https://doi.org/10.1021/acs.jproteome.5b00109

Mal, T.K., and M. Ikura. 2008. NMR investigation of calmodulin. In Modern Magnetic Resonance. G.A.Webb, editor. Springer. Dordrecht. 503–516. https://doi.org/10.1007/1-4020-3910-7_63

McCoy, A.J., R.W. Grosse-Kunstleve, P.D. Adams, M.D. Winn, L.C. Storoni, and R.J. Read. 2007. Phaser crystallographic software. *J. Appl. Cryst.* 40:658–674. https://doi.org/10.1107/S0021889807021206

Mehta, A., Y. Shirai, E. Kouyama-Suzuki, M. Zhou, T. Yoshizawa, T. Yanagawa, T. Mori, and K. Tabuchi. 2021. IQSEC2 deficiency results in abnormal social behaviors relevant to autism by affecting functions of neural circuits in the medial prefrontal cortex. *Cells.* 10:2724. https://doi.org/10.3390/cells10102724

Mignot, C., A.C. McMahon, C. Bar, P.M. Campeau, C. Davidson, J. Buratti, C. Nava, M.-L. Jacquemont, M. Tallot, M. Milh, et al. 2019. IQSEC2-related encephalopathy in males and females: A comparative study including 37 novel patients. *Genet. Med.* 21:837–849. https://doi.org/10.1038/s41436-018-0268-1

Monies, D., M. Abouelhoda, M. Assoum, N. Moghrabi, R. Rafiullah, N. Almontashiri, M. Alowain, H. Alzaidan, M. Alsayed, S. Subhani, et al. 2019. Lessons learned from large-scale, first-tier clinical exome sequencing in a highly consanguineous population. *Am. J. Hum. Genet.* 104:1182–1201. https://doi.org/10.1016/j.ajhg.2019.04.011

Morleo, M., D. Iaconis, D. Chitayat, I. Peluso, R. Marzella, A. Renieri, F. Mari, and B. Franco. 2008. Disruption of the IQSEC2 transcript in a female with X;autosome translocation t(X;20)(p11.2;q11.2) and a phenotype resembling X-linked infantile spasms (ISSX) syndrome. *Mol. Med. Rep.* 1:33–39. https://doi.org/10.3892/mmr.1.1.33

Murphy, J.A., O.N. Jensen, and R.S. Walikonis. 2006. BRAG1, a Sec7 domain-containing protein, is a component of the postsynaptic density of excitatory synapses. *Brain Res.* 1120:35–45. https://doi.org/10.1016/j.brainres.2006.08.096

Myers, K.R., G. Wang, Y. Sheng, K.K. Conger, J.E. Casanova, and J.J. Zhu. 2012. Arf6-GEF BRAG1 regulates JNK-mediated synaptic removal of GluA1-containing AMPA receptors: A new mechanism for nonsyndromic X-linked mental disorder. *J. Neurosci.* 32:11716–11726. https://doi.org/10.1523/JNEUROSCI.1942-12.2012

Nawrotek, A., S. Benabdi, S. Niyomchon, M.H. Kryszke, C. Ginestier, T. Cañeque, L. Tepshi, A. Mariani, R.P. St Onge, G. Giaever, et al. 2019. PH-

domain-binding inhibitors of nucleotide exchange factor BRAG2 disrupt Arf GTPase signaling. *Nat. Chem. Biol.* 15:358–366. https://doi.org/10.1038/s41589-019-0228-3

Otwinowski, Z., and W. Minor. 1997. Processing of X-ray diffraction data collected in oscillation mode. *Methods Enzymol.* 276:307–326. https://doi.org/10.1016/S0076-6879(97)76066-X

Radley, J.A., R.B.G. O'Sullivan, S.E. Turton, H. Cox, J. Vogt, J. Morton, E. Jones, S. Smithson, K. Lachlan, J. Rankin, et al. 2019. Deep phenotyping of 14 new patients with IQSEC2 variants, including monozygotic twins of discordant phenotype. *Clin. Genet.* 95:496–506. https://doi.org/10.1111/cge.13507

Rogers, E.J., R. Jada, K. Schragenheim-Rozales, M. Sah, M. Cortes, M. Florence, N.S. Levy, R. Moss, R.S. Walikonis, R. Palty, et al. 2019. An IQSEC2 mutation associated with intellectual disability and autism results in decreased surface AMPA receptors. *Front. Mol. Neurosci.* 12:43. https://doi.org/10.3389/fnmol.2019.00043

Sah, M., A.N. Shore, S. Petri, A. Kanber, M. Yang, M.C. Weston, and W.N. Frankel. 2020. Altered excitatory transmission onto hippocampal interneurons in the IQSEC2 mouse model of X-linked neurodevelopmental disease. *Neurobiol. Dis.* 137:104758. https://doi.org/10.1016/j.nbd.2020.104758

Sakagami, H., M. Sanda, M. Fukaya, T. Miyazaki, J. Sukegawa, T. Yanagisawa, T. Suzuki, K. Fukunaga, M. Watanabe, and H. Kondo. 2008. IQ-ArfGEF/BRAG1 is a guanine nucleotide exchange factor for Arf6 that interacts with PSD-95 at postsynaptic density of excitatory synapses. *Neurosci. Res.* 60:199–212. https://doi.org/10.1016/j.neures.2007.10.013

Scholz, R., S. Berberich, L. Rathgeber, A. Kolleker, G. Köhr, and H.C. Kornau. 2010. AMPA receptor signaling through BRAG2 and Arf6 critical for long-term synaptic depression. *Neuron.* 66:768–780. https://doi.org/10.1016/j.neuron.2010.05.003

Shoubridge, C., T. Dudding-Byth, L. Pasquier, H. Goel, P. Yap, and V. McConnell. 2022. IQSEC2-related encephalopathy in males due to missense variants in the pleckstrin homology domain. *Clin. Genet.* 102:72–77. https://doi.org/10.1111/cge.14136

Shoubridge, C., R.J. Harvey, and T. Dudding-Byth. 2019. IQSEC2 mutation update and review of the female-specific phenotype spectrum including intellectual disability and epilepsy. *Hum. Mutat.* 40:5–24. https://doi.org/10.1002/humu.23670

Shoubridge, C., P.S. Tarpey, F. Abidi, S.L. Ramsden, S. Rujirabanjerd, J.A. Murphy, J. Boyle, M. Shaw, A. Gardner, A. Proos, et al. 2010. Mutations in the guanine nucleotide exchange factor gene IQSEC2 cause nonsyndromic intellectual disability. *Nat. Genet.* 42:486–488. https://doi.org/10.1038/ng.588

Someya, A., M. Sata, K. Takeda, G. Pacheco-Rodriguez, V.J. Ferrans, J. Moss, and M. Vaughan. 2001. ARF-GEP(100), a guanine nucleotide-exchange protein for ADP-ribosylation factor 6. *Proc. Natl. Acad. Sci. USA.* 98:2413–2418. https://doi.org/10.1073/pnas.051634798

Uezu, A., D.J. Kanak, T.W.A. Bradshaw, E.J. Soderblom, C.M. Catavero, A.C. Burette, R.J. Weinberg, and S.H. Soderling. 2016. Identification of an elaborate complex mediating postsynaptic inhibition. *Science.* 353:1123–1129. https://doi.org/10.1126/science.aag0821

Um, J.W., G. Choii, D. Park, D. Kim, S. Jeon, H. Kang, T. Mori, T. Papadopoulos, T. Yoo, Y. Lee, et al. 2016. IQ motif and SEC7 domain-containing protein 3 (IQSEC3) interacts with gephyrin to promote inhibitory synapse formation. *J. Biol. Chem.* 291:10119–10130. https://doi.org/10.1074/jbc.M115.712893

Wayhelova, M., M. Ryzí, J. Oppelt, E. Hladilkova, V. Vallova, L. Krskova, M. Vilemova, H. Polackova, R. Gaillyova, and P. Kuglik. 2020. Novel familial IQSEC2 pathogenic sequence variant associated with neurodevelopmental disorders and epilepsy. *Neurogenetics.* 21:269–278. https://doi.org/10.1007/s10048-020-00616-3

Yang, H., L. Shi, B.A. Wang, D. Liang, C. Zhong, W. Liu, Y. Nie, J. Liu, J. Zhao, X. Gao, et al. 2012a. Generation of genetically modified mice by oocyte injection of androgenetic haploid embryonic stem cells. *Cell.* 149:605–617. https://doi.org/10.1016/j.cell.2012.04.002

Yang, Y., X. Shu, D. Liu, Y. Shang, Y. Wu, L. Pei, X. Xu, Q. Tian, J. Zhang, K. Qian, et al. 2012b. EPAC null mutation impairs learning and social interactions via aberrant regulation of miR-124 and Zif268 translation. *Neuron.* 73:774–788. https://doi.org/10.1016/j.neuron.2012.02.003

Zhang, M., T. Tanaka, and M. Ikura. 1995. Calcium-induced conformational transition revealed by the solution structure of apo calmodulin. *Nat. Struct. Biol.* 2:758–767. https://doi.org/10.1038/nsb0995-758

Zhong, C., Q. Yin, Z. Xie, M. Bai, R. Dong, W. Tang, Y.H. Xing, H. Zhang, S. Yang, L.L. Chen, et al. 2015. CRISPR-Cas9-mediated genetic screening in mice with haploid embryonic stem cells carrying a guide RNA library. *Cell Stem Cell.* 17:221–232. https://doi.org/10.1016/j.stem.2015.06.005

Supplemental material

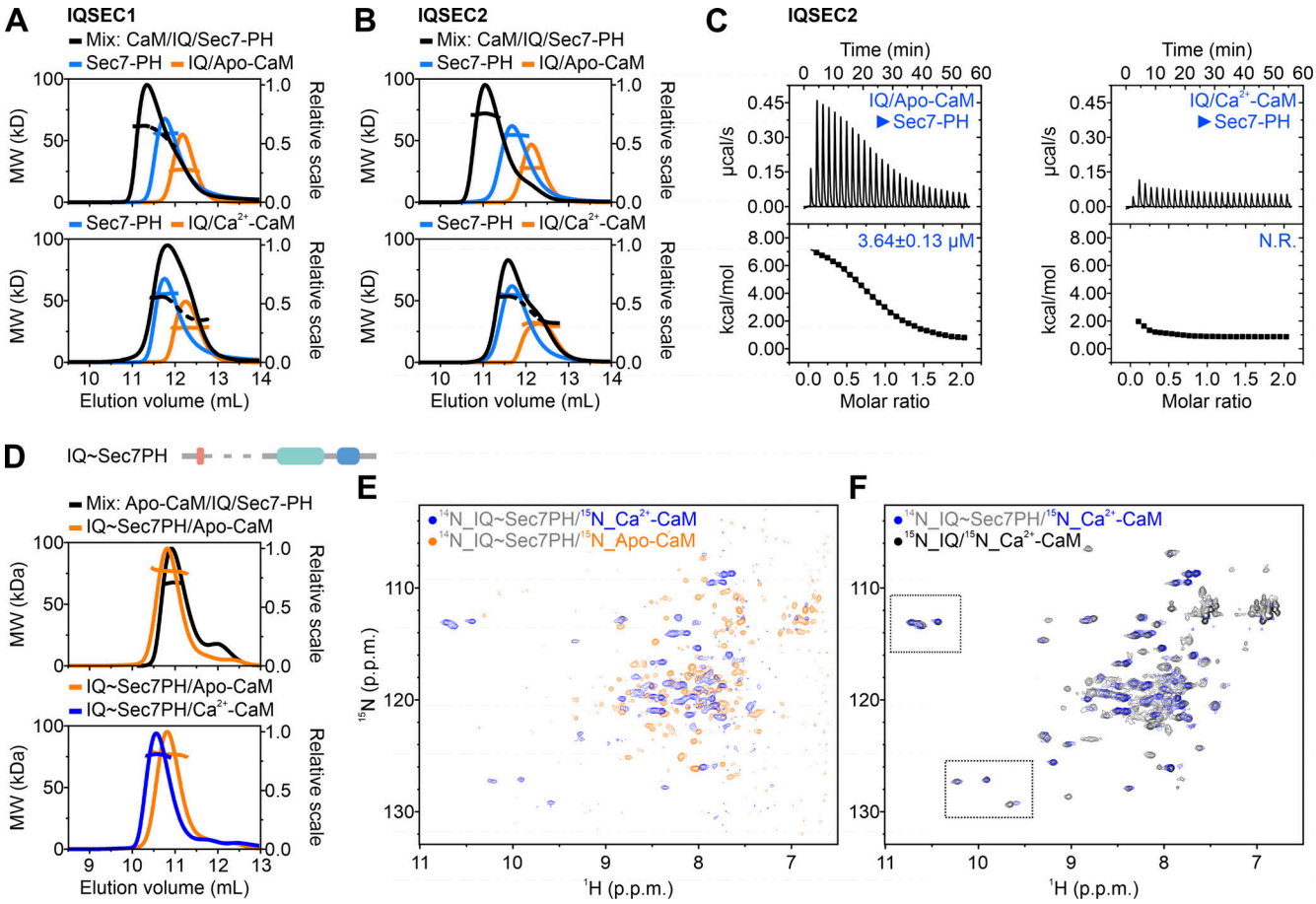

Figure S1. **The IQ-motif/CaM complex is coupled with the Sec7-PH tandem in IQSECs and dissociated by Ca^{2+}. (A)** The SEC-MALS analysis of the IQ-motif/CaM complex, the Sec7-PH tandem of IQSEC1, and their mixture. **(B)** The SEC-MALS analysis of the IQ-motif/CaM complex, the Sec7-PH tandem of IQSEC2, and their mixture. **(C)** The ITC curve of 200 μM IQ-motif/CaM complex titrating into 20 μM Sec7-PH protein of IQSEC2 in the absence and presence of Ca^{2+}. The ITC titration was performed at 10°C so that the reaction had an obvious heat change. N.R., fitting is not reliable. **(D)** The SEC-MALS analysis shows different elution volumes of the IQ~Sec7PH/CaM complexes in the absence and presence of Ca^{2+}. The IQ~Sec7PH/Apo-CaM complex is well-aligned with the Apo-CaM/IQ/Sec7-PH mixture. **(E)** Superposition plot of ^{1}H, ^{15}N HSQC spectra of the ^{14}N_IQ~Sec7PH/^{15}N_CaM complexes in the absence (orange), and presence of Ca^{2+} (blue). **(F)** Superposition plot of ^{1}H, ^{15}N HSQC spectra of the ^{14}N_IQ~Sec7PH/^{15}N_Ca^{2+}-CaM complexes (blue) and the ^{15}N_IQ/^{15}N_Ca^{2+}-CaM complexes (black). Two black dotted rectangles are expanded in Fig. 1 E.

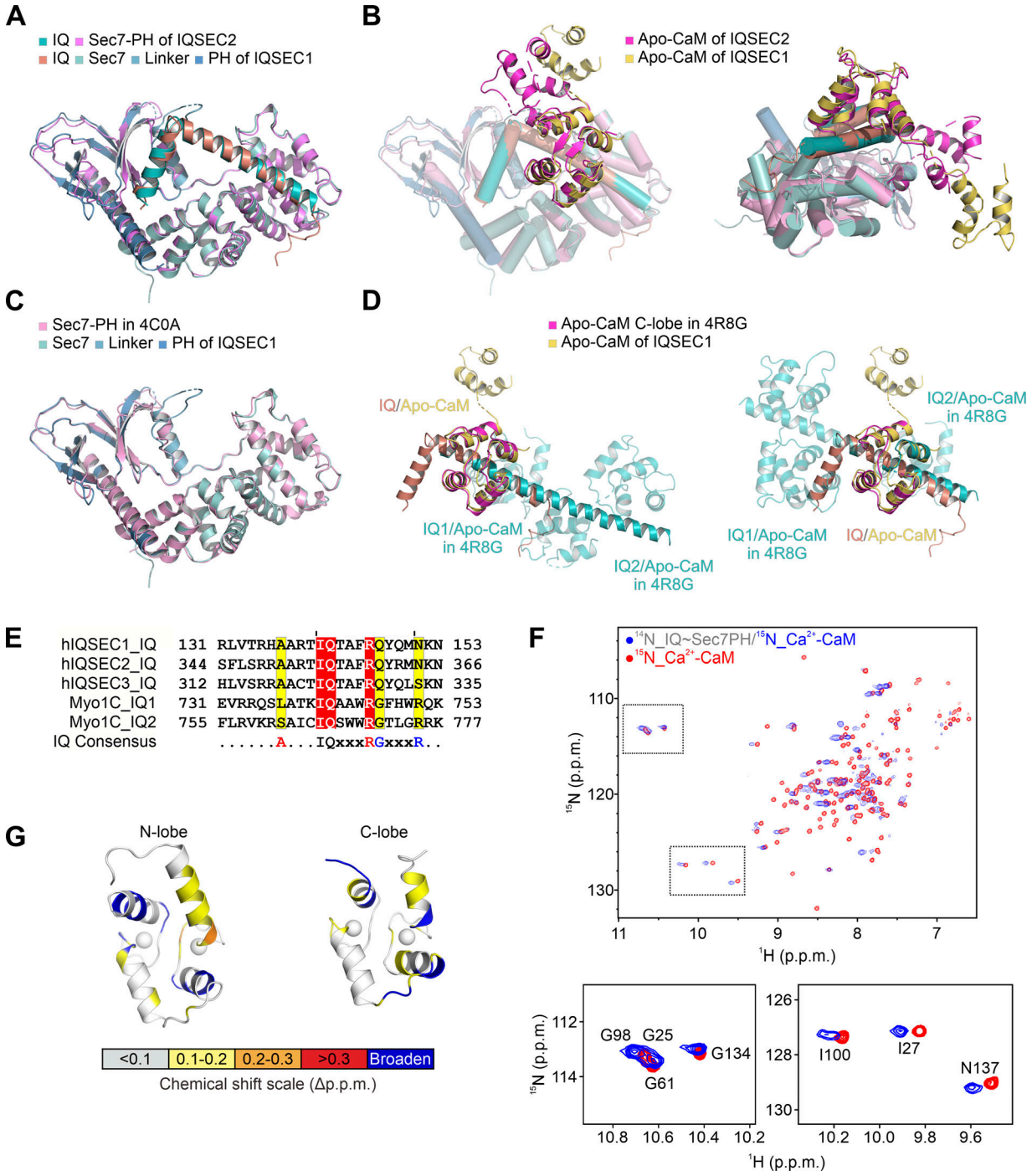

Figure S2. **Comparisons of the Apo-CaM/IQ/Sec7-PH ternary structure with those of related proteins. (A and B)** Superposition of the Apo-CaM/IQ/Sec7-PH ternary complex structure of IQSEC1 with that of IQSEC2. Panel A only shows the superposition of the two IQ/Sec7-PH complexes. Panel B shows the superposition of the two overall structures. **(C)** Superposition of the Sec7-PH structures from the Apo-CaM/IQ/Sec7-PH ternary complex structure with that from the ARF1/Sec7-PH complex structure (PDB accession no. 4C0A). **(D)** Superposition of the IQ/Apo-CaM structure from the Apo-CaM/IQ/Sec7-PH ternary complex with the IQ1/Apo-CAM (left) or IQ2/Apo-CaM (right) structure from the myosin-1c/Apo-CaM complex (PDB accession no. 4R8G). **(E)** Sequence alignment analysis of the IQ-motifs from IQSECs and IQ-motifs from myosin-1c. **(F)** Superposition plot of the ^{1}H, ^{15}N HSQC spectrum of the ^{14}N_IQ~Sec7PH/^{15}N_Ca^{2+}-CaM complexes of IQSEC3 (blue) with that of ^{15}N_Ca^{2+}-CaM (red), showing that Ca^{2+}-CaM experienced IQ~Sec7PH binding-induced conformational changes. Two black dotted rectangles are expanded in the lower panel. The assignments of the peaks corresponding to the ^{15}N_Ca^{2+}-CaM are labeled. **(G)** Mapping of the backbone amide chemical shift changes of the N- and C-lobes of Ca^{2+}-CaM resulted from the CaM/IQ/Sec7-PH coupling. The result indicates that both lobes of Ca^{2+}-CaM are engaged in binding to IQ~Sec7PH. The analysis was performed by comparing the ^{1}H, ^{15}N HSQC spectra as shown in F. The chemical shift difference of each peak is defined as Δp.p.m. = $[(\Delta\delta HN)^2 + (\alpha N * \Delta\delta HN)^2]^{1/2}$. The scaling factor (αN) used to normalize the ^{1}H and ^{15}N chemical shifts is 0.17.

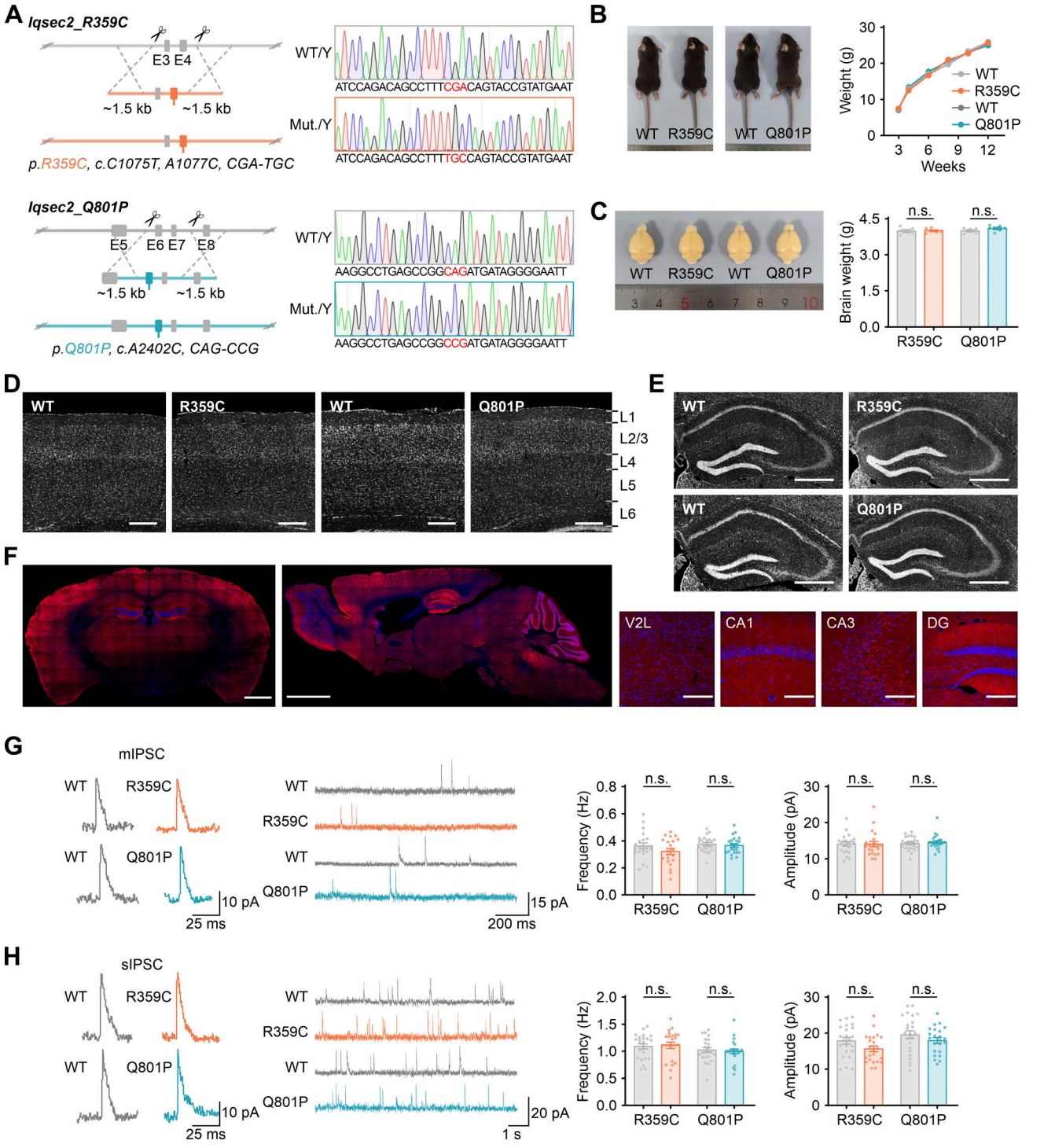

Figure S3. **Generation and characterization of *mScarlet-Iqsec2*, IQSEC2 R359C, and IQSEC2 Q801P mice. (A)** Schematic strategies for generating *Iqsec2* mutant mice using CRISPR/Cas9. sgRNA recognition sites are indicated with scissors. Representative DNA sequencing results from WT and hemizygous mice highlighted substituted sequences. **(B)** Representative gross appearances and growth chart plots of the R359C and Q801P mutant mice compared with their respective WT control littermates. Data are presented as mean ± SEM (n = 10–15 mice per group). **(C)** Representative brain photographs and plots of adult mouse brain weights. Data are presented as mean ± SEM (n = 23–25 mice per group; n.s., not significant; unpaired t test). **(D and E)** Overall cellular structures in the hippocampus and the somatosensory area of the cerebral cortex of the R359C and Q801P mutant mice and their WT littermates were assessed by DAPI staining. Scale bars, 200 µm. **(F)** Representative fluorescence images of coronal and sagittal sections from *mScarlet-Iqsec2* adult mouse brains. Nuclei were stained with DAPI (blue). V2L, secondary visual cortex, lateral area; CA1 and CA3, Ammon's horn 1 and three of the hippocampus; DG, dentate gyrus. Scale bars, coronal and sagittal sections: 1 mm; V2L: 125 µm; CA1 and CA3: 100 µm; DG: 200 µm. **(G and H)** The R359C and the Q801P mice show normal inhibitory synaptic transmissions. Representative traces and plots showing the frequency and the mean amplitude of the miniature and the spontaneous IPSCs recorded from CA1 pyramidal neurons in the slices from the R359C and Q801P mutant mice and their respective WT control littermates. Data are presented as mean ± SEM (n = 21–23 recordings per eight mice per group; n.s., not significant; unpaired t test).

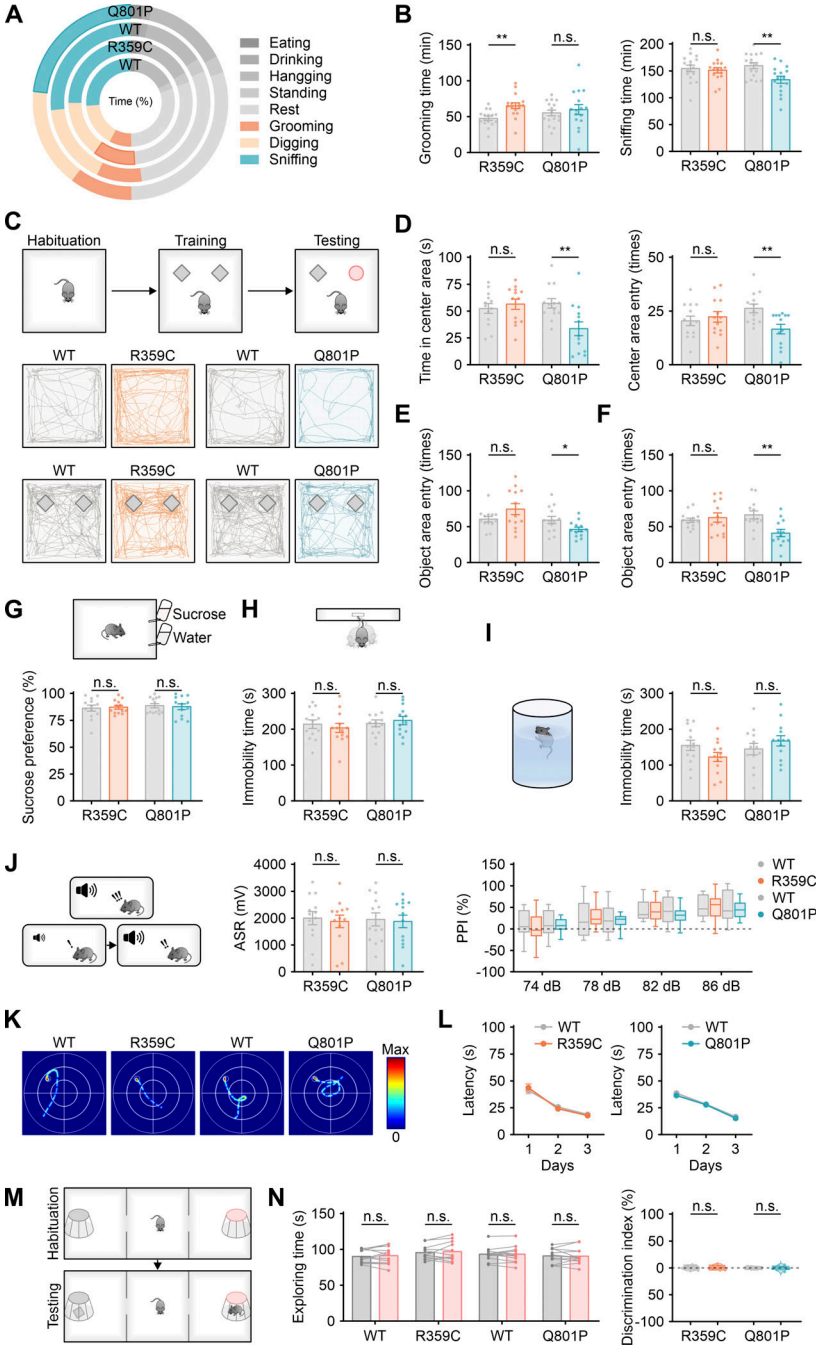

Figure S4. **Behavioral phenotypes of the R359C and the Q801P mice. (A)** Pie chart summary showing 48 h natural spontaneous behavior recording of the R359C and Q801P mutant mice as well as their respective WT control littermates at 60 ± 2 d old of age. **(B)** Bar graphs showing the grooming and sniffing time in the 48 h natural spontaneous behavior recording. Data are presented as mean ± SEM (n = 16 mice per group; n.s., not significant; **P < 0.01; unpaired t test). **(C)** Schematic representation of the novel object recognition task and representative exploration trajectories during the habituation and training phase of individual mice. **(D)** Bar graphs showing the time spent and the number of entrances in the center area during the habituation phase. Data are presented as mean ± SEM (n = 13 mice per group; **P < 0.01; unpaired t test). **(E and F)** Bar graphs showing the number of entrances in the object around the area during the training and testing phases. Related to Fig. 6, A and B. Data are presented as mean ± SEM (n = 13 mice per group; *P < 0.05; **P < 0.01; unpaired t test). **(G–I)** Bar graphs showing the performance of the R359C and Q801P mutant and their WT control littermate mice in the sucrose preference, tail suspending, and forced swimming tests. Data are presented as mean ± SEM (n = 13 mice per group; n.s., not significant; unpaired t test). **(J)** Measurement of the acoustic startle reflex (ASR) and prepulse inhibition (PPI) of the R359C and Q801P mutant and their WT control littermate mice. Data are presented as mean ± SEM (n = 13 mice per group; n.s., not significant; unpaired t test). **(K)** Representative exploration trajectories on the third day during the visible platform task in the Morris water maze. **(L)** The escape latency in the Morris water maze to reach the visible platform. Data are presented as mean ± SEM (n = 13 mice per group; n.s., not significant; unpaired t test). **(M)** Schematic representation of the three-chamber tests. **(N)** Left: Bar graphs showing the time spent exploring the left (gray) and right (red) chambers during the habituation phase of individual mice. Right: No preference on location in three-chamber tests as shown by the discrimination index showing by violin plots. Data are presented as median, quartiles, and individual values (n = 12–13 mice per group; n.s., not significant; left: paired t test; right: unpaired t test).

Provided online is Table S1. Table S1 lists statistical data summary.